The Basic Properties of the Electronic Structure of the Oxygen-evolving Complex of Photosystem II Are Not Perturbed by Ca^{2+} Removal*[S]

Thomas Lohmiller[‡1], **Nicholas Cox**[‡], **Ji-Hu Su**[‡2], **Johannes Messinger**[§3], **and Wolfgang Lubitz**[‡4]

From the ‡Max-Planck-Institut für Bioanorganische Chemie, Stiftstrasse 34-36, 45470 Mülheim an der Ruhr, Germany and the §Department of Chemistry, Chemical Biological Centre (KBC), Umeå University, S-90187 Umeå, Sweden

Background: EPR/^{55}Mn ENDOR spectroscopy of the oxygen-evolving complex (OEC) and Mn^{2+} in Ca^{2+}-depleted photosystem II.
Results: Electronic model of the Ca^{2+}-depleted OEC; characterization of Mn^{2+} binding.
Conclusion: Ca^{2+} is not critical for maintaining the electronic and spatial structure of the OEC. Its removal exposes a Mn^{2+} binding site supposedly in an extrinsic subunit.
Significance: Mechanistic implications for water oxidation; Mn^{2+} in photoassembly/D1 protein repair.

Ca^{2+} is an integral component of the Mn$_4$O$_5$Ca cluster of the oxygen-evolving complex in photosystem II (PS II). Its removal leads to the loss of the water oxidizing functionality. The S$_2'$ state of the Ca^{2+}-depleted cluster from spinach is examined by X- and Q-band EPR and ^{55}Mn electron nuclear double resonance (ENDOR) spectroscopy. Spectral simulations demonstrate that upon Ca^{2+} removal, its electronic structure remains essentially unaltered, *i.e.* that of a manganese tetramer. No redistribution of the manganese valence states and only minor perturbation of the exchange interactions between the manganese ions were found. Interestingly, the S$_2'$ state in spinach PS II is very similar to the native S$_2$ state of *Thermosynechococcus elongatus* in terms of spin state energies and insensitivity to methanol addition. These results assign the Ca^{2+} a functional as opposed to a structural role in water splitting catalysis, such as (i) being essential for efficient proton-coupled electron transfer between Y$_Z$ and the manganese cluster and/or (ii) providing an initial binding site for substrate water. Additionally, a novel ^{55}Mn^{2+} signal, detected by Q-band pulse EPR and ENDOR, was observed in Ca^{2+}-depleted PS II. Mn^{2+} titration, monitored by ^{55}Mn ENDOR, revealed a specific Mn^{2+} binding site with a submicromolar K_D. Ca^{2+} titration of Mn^{2+}-loaded, Ca^{2+}-depleted PS II demonstrated that the site is reversibly made accessible to Mn^{2+} by Ca^{2+} depletion and reconstitution. Mn^{2+} is proposed to bind at one of the extrinsic subunits. This process is possibly relevant for the formation of the Mn$_4$O$_5$Ca cluster during photoassembly and/or D1 repair.

The oxygen-evolving complex (OEC)[5] of photosystem II (PS II) catalyzes the light-driven oxidation of water. The OEC contains an inorganic Mn$_4$O$_5$Ca metallocofactor that includes five μ-oxo bridge linkages and is coordinated by a framework of surrounding amino acids (1–6) in a highly defined manner that confers catalytic function. The redox-active tyrosine residue Y$_Z$ (D1-Tyr-161) enables electron transfer from the Mn$_4$O$_5$Ca cluster to P$_{680}$$^+$, the radical cation formed upon photon absorption and charge separation. The Mn$_4$O$_5$Ca cluster undergoes four successive oxidations, cycling through a series of different net valence states, referred to as the S$_i$ states (where $i = 0-4$ denotes the number of oxidizing equivalents stored in the cluster). The transient state S$_4$ spontaneously returns to S$_0$ upon regaining four electrons from the two substrate water molecules, which in the process form molecular oxygen. The release of O$_2$ is followed by the rebinding of at least one H$_2$O molecule (for reviews, see Refs. 7–14).

X-ray crystallographic structures of the PS II protein complex provided an atomic picture of the structure of the OEC (1–6), identifying all amino acids that ligate the Mn$_4$O$_5$Ca cluster. The metallocofactor resembles a distorted chair, consisting of the cuboidal moiety Mn$_3$O$_3$Ca (Mn$_{B3}$Mn$_{C2}$Mn$_{D1}$),[6] with the fourth, outer manganese ion (Mn$_{A4}$), connected to the cuboid via an additional μ-oxo bridge (O4) to one of the manganese vertices (Mn$_{B3}$). The reported cluster is likely modified due to photoreduction of the Mn^{III} and Mn^{IV} ions, such that the Mn-Mn and Mn-Ca distances seen in the x-ray structure are all elongated as compared with those derived from extended x-ray absorption fine structure (EXAFS) measurements (15). Allowing for this, the basic topology of the x-ray structure is similar to earlier literature models, including the geometry-optimized

---

Electronic Structure of the Ca^{2+}-depleted OEC of Photosystem II
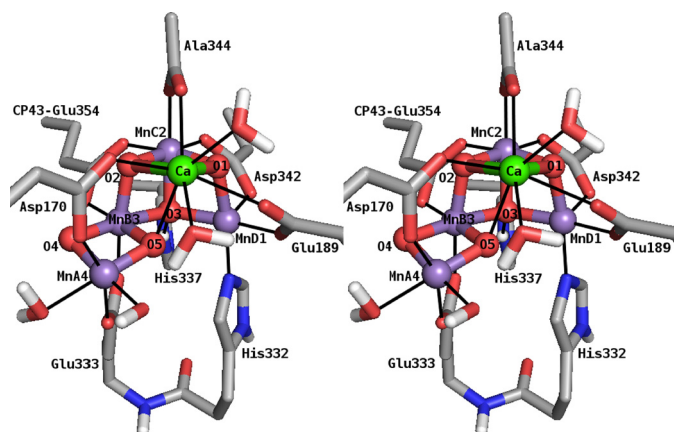

FIGURE 1. **Stereo view of a DFT model of the Mn$_4$O$_5$Ca cluster in the S$_2$ state and directly ligating amino acid residues and H$_2$O/OH$^-$ molecules (18).** Amino acids, except CP43-Glu-354, are from PS II subunit D1. Manganese, calcium, nitrogen, oxygen, carbon, and hydrogen atoms are shown in *purple*, *green*, *blue*, *red*, *gray*, and *white*, respectively. Nonpolar H atoms are omitted for clarity.

density functional theory (DFT) models of Kusunoki (16), Siegbahn (17), and the recent model of Ames *et al.* (18), in which the cuboid exhibits an open conformation with Mn$_{A4}$ connected to Mn$_{B3}$ via a di-μ-oxo bridge (Fig. 1).

The Ca^{2+} ion of the Mn$_4$O$_5$Ca cluster, which can be removed from and reconstituted into the OEC (19–21), is essential for catalytic function (19–23). The non-catalytic Ca^{2+}-depleted OEC cannot complete the S state cycle, advancing only to a modified S$_2$ state, termed S$_2'$ (24, 25). The reason for this remains unclear. However, four basic explanations exist in the current literature based on the proposed role(s) for the Ca^{2+} ion during the S state cycle (for reviews, see Refs. 26–28). These include the following: (i) As an integral component of the OEC (6), the Ca^{2+} ion can be suspected to be of crucial structural importance. However, EXAFS experiments suggest that Ca^{2+} depletion leads to only a small spatial reorganization of the remnant Mn$_4$O$_5$ cluster (29). (ii) It facilitates fast one-electron transfer from the OEC to Y$_Z^+$ (for reviews, see Refs. 11 and 30). The formation of the S$_2'$ state requires long visible light illumination at temperatures $\geq$0 °C. This is in contrast to the native S$_2$ state, which can be generated via visible light illumination at −78 °C. This apparent increase in the activation energy of OEC turnover upon Ca^{2+} removal may represent a decoupling of the Y$_Z^+$ from the OEC, such that Ca^{2+}-mediated protein conformational changes and/or H$^+$ translocations associated with physiological S state transitions are blocked. (iii) It is a binding/staging site for substrate water and its deprotonation (26, 31). The kinetics of substrate water binding to the OEC are affected by biochemical exchange of Ca^{2+} with Sr^{2+}, the only surrogate ion able to confer catalytic activity (19, 23, 32). It can presumably act in place of Ca^{2+} as it has approximately the same size and a similar Lewis acidity (31). This result has been interpreted as evidence for Ca^{2+} binding one of the substrate waters. Inhibition due to Ca^{2+} depletion would then reflect the loss of a substrate binding site. (iv) Although the basic structural arrangement of manganese ions in the cluster is retained upon Ca^{2+} removal, it is uncertain if their magnetic and/or electronic interactions are perturbed, which could lead to a decoupling of the cluster or a rearrangement of the manganese valence states. Thus, Ca^{2+} depletion could potentially change the redox properties as well as substrate and/or protein interactions of the complex, inhibiting catalytic function.

The Mn$_4$O$_5$Ca cluster in the S$_2$ state exhibits a characteristic multiline EPR signal centered at $g \approx 2$ (33) that arises from an $S = 1/2$ ground spin state of the cluster. Under certain conditions (illumination, reactants), additional signals are observed at higher g values; in spinach, a second broad signal can be detected at $g \approx 4.1$ (34, 35), attributed to an $S = 5/2$ spin state (36). These signals are affected by the presence of small alcohols, foremost methanol (MeOH) (37–41), which enhance the intensity of the multiline signal at the expense of the $g \approx 4.1$ signal (37) (for a full discussion see Ref. 41). The Mn$_4$O$_5$ cluster in the S$_2'$ state also exhibits a multiline signal; however, its hyperfine splitting pattern is perturbed. It contains a larger number of resolved lines as compared with the native S$_2$ multiline signal, with a smaller average line spacing (5.5–6 *versus* 8.8 mT). The magnetic interaction between Y$_Z^\bullet$ and the OEC is also perturbed in Ca^{2+}-depleted PS II as evidenced by changes in the tyrosine split signal of the S$_2'$Y$_Z^\bullet$ state (24, 25).

A detailed understanding of the electronic structure of the Mn$_4$O$_5$Ca cluster in the S$_2$ state has been developed from pulse EPR data (42–46), in particular ^{55}Mn electron nuclear double resonance (ENDOR). These experiments demonstrated that the four manganese ions contribute about equally to the ground electronic state of the S$_2$ state; *i.e.* all four manganese ions carry approximately the same spin density. This requirement allows an assessment of the electronic exchange interactions between the four manganese ions and the development of Mn$_4$ coupling schemes. These necessarily reflect the geometric structure of the OEC and allow the assignment of the individual manganese oxidation states. Our recently proposed model for the S$_2$ state (18) is described under "Discussion." This scheme places the only Mn^{III} ion inside the cuboidal unit (Mn$_{D1}$) (see also Ref. 47) and compares favorably with information from complementary spectroscopic measurements (48–50).

Although it has not been directly observed by EPR spectroscopy, the possibility of another paramagnetic manganese species being able to bind to the Ca^{2+}-depleted PS II has been suggested in an earlier study by Booth *et al.* (51). The additional species was suggested to be a Mn^{2+} ion that can bind specifically to a site in the protein complex that is created or becomes accessible via structural changes in the course of Ca^{2+} removal. This was based on the observation that, after equimolar amounts of Mn^{2+} ions had been added to Ca^{2+}-depleted PS II, no Mn^{2+} was observed by X-band continuous wave (CW) EPR. Upon titrating Ca^{2+} ions back into these samples, Mn^{2+} was released as seen from the appearance of the six-line Mn^{2+} EPR signal.

In this work, both the spin system of the Mn$_4$O$_5$ cluster in the S$_2'$ state of Ca^{2+}-depleted PS II and the binding of Mn^{2+} ions to this protein were studied by EPR and ENDOR spectroscopy at X- and Q-band frequencies. The results provide new insight into the role of the Ca^{2+} ion in the native OEC.

TABLE 1

Oxygen evolution activities and relative S_2 multiline EPR signal intensities of the Ca²⁺-containing native, the Ca²⁺-depleted, and the Ca²⁺-reconstituted PS II membrane preparations from spinach

Observable	Native	Ca²⁺-depleted	Ca²⁺-reconstituted
Enzymatic rates/μmol O_2/mg chlorophyll/h[a]	390 ± 30	27 ± 1	330 ± 30
Relative enzymatic rates	100%	7 ± 0%	84 ± 8%
Relative S_2 state multiline signal intensities[b]	100%	8 ± 3%	105 ± 12%

[a] Determined as an average of at least 8 single measurements at a minimum of 2 different chlorophyll concentrations from 5 to 25 μg/ml.

[b] Determined from the peak-to-trough distances of four prominent derivative peaks in the CW EPR spectrum (100).

EXPERIMENTAL PROCEDURES

Sample Preparation—PS II-enriched thylakoid membranes were prepared from spinach based on the procedure of Berthold *et al.* (52) using detergent treatment by incubation with Triton X-100 for 15 min. All work was performed in the dark or very dim green light, and the PS II was kept at 4 °C before storage in the dark at −80 °C or in liquid N_2. Chlorophyll concentrations were determined by assays using aqueous acetone (80%) extracts (53) with updated extinction coefficients (54) using an ATI Unicam UV-visible spectrometer UV2–300.

Ca²⁺ depletion and reconstitution based on the low pH/citrate treatment method (21) was achieved as described previously (55). The final buffer used was 50 mM MES, 15 mM NaCl, 0.4 M sucrose, 1 mM EDTA, pH 6.5. Ca²⁺ removal and, as a proof for the integrity of the OEC, Ca²⁺ rebinding was confirmed both by enzymatic assays and by X-band CW EPR. The O_2 evolution rates of native PS II were ~400 μmol O_2/mg of chlorophyll/h (see the following section). O_2 evolution rates dropped to 5–10% in Ca²⁺-depleted and were reactivated to >80% in Ca²⁺-reconstituted samples. Similar percentages of the S_2 multiline signal were observed after white light illumination with a tungsten lamp through an aqueous 5% $CuSO_4$ IR filter of the respective samples at 200 K for 5 min (Table 1, Fig. 2A). These numbers are consistent with previous literature reports (25, 29, 56).

Advancement of dark-adapted $S_1{}'$ state EPR samples to the $S_2{}'$ and $S_2{}'Y_Z{}^\bullet$ states (25) was done by illumination at 0 °C for 3 min, with 125 μM 3-(3,4-dichlorophenyl)-1,1-dimethylurea (10 mM in dimethyl sulfoxide) added to the samples advanced to the $S_2{}'$ state, which restricts the acceptor site and, thus, Y_Z to one turnover.

For Ca²⁺ and Mn²⁺ titration experiments, dark-adapted Ca²⁺-depleted PS II membranes were rebuffered in EDTA-free buffer by three cycles of dilution, centrifugation at 39,000 × g for 15 min, and resuspension using 50 mM MES, 15 mM NaCl, 5 mM $MgCl_2$, 0.4 M sucrose, pH 6.5. The final concentration of PS II reaction centers (RCs) in the samples was 28 ± 3 μM based on a chlorophyll concentration of 6.3 ± 0.8 mg ml⁻¹ and assuming 250 chlorophylls/RC (57) after 15 min Triton X-100 treatment. The samples were incubated with known amounts of Mn²⁺ ranging from 0 to 4 eq per RC for 2 h. For the Ca²⁺ titration, samples containing 0.8 added eq of Mn²⁺ were incubated with known amounts of Ca²⁺ between 0 and 2400 eq for one additional hour. Mn²⁺ and Ca²⁺ ions were added from stock solutions of their chlorides.

Oxygen Evolution Measurements—Steady state PS II enzyme activity at 25 °C was determined by polarographic measurement of the O_2 concentration in a PS II-containing assay mixture using a Clark-type Hansatech oxygen electrode with a high
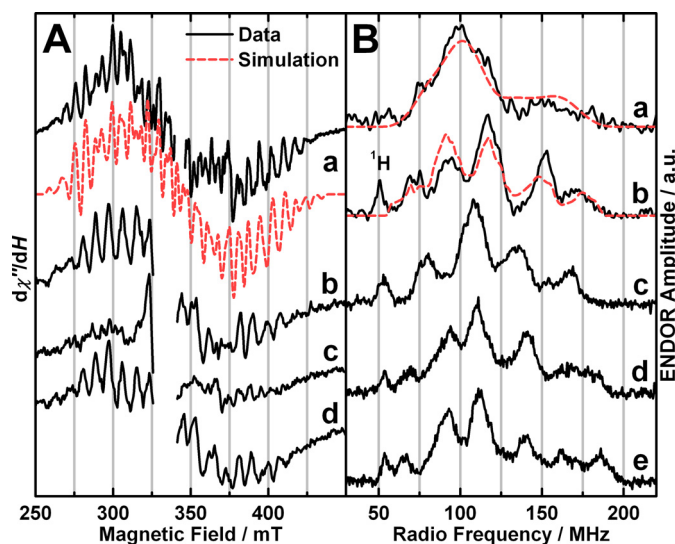

FIGURE 2. **EPR and ENDOR experimental spectra (*black solid traces*) and simulations (*red dashed traces*).** *A*, X-band CW EPR of PS II isolated from spinach. Shown are the Ca²⁺-depleted OEC poised in the $S_2{}'$ state (*a*) and the native (*b*), Ca²⁺-depleted (*c*), and the Ca²⁺-reconstituted OECs (*d*) illuminated at 200 K. In the experimental spectrum, the region of the overlapping $Y_D{}^\bullet$ signal (*g* ≈ 2) was omitted for clarity. In *a*, a fourth order polynomial, and in *b–d*, a background signal of the resonator cavity were subtracted from the raw data. Experimental parameters: MW frequencies, 9.634 GHz (*a*), 9.44 GHz (*b–d*); MW power, 0.5 milliwatt (*a*), 20 milliwatts (*b–d*); modulation amplitude, 7.5 G (*a*), 15 G (*b–d*); time constant, 82 ms; temperature, 8 K (*a*), 10 K (*b–d*). *B*, X-band (*a*) and Q-band (*b–e*) Davies ENDOR of the Ca²⁺-depleted $S_2{}'$ state from spinach compared with the native and Sr²⁺-substituted S_2 states from spinach and *T. elongatus*. Shown are Ca²⁺-depleted Mn_4O_5 $S_2{}'$, spinach (*a* and *b*), native Mn_4O_5Ca S_2, spinach (taken from Refs. 45 and 46) (*c*), native Mn_4O_5Ca S_2, *T. elongatus* (from Ref. 49) (*d*), and Sr²⁺-substituted Mn_4O_5Sr S_2, *T. elongatus* (from Ref. 49) (*e*). *a* and *b* were smoothed using a 9- and 5-point moving average, respectively. *b* is the difference of an $S_2{}'$ state spectrum after illumination at 0 °C minus an $S_1{}'$ state spectrum after dark adaptation (supplemental Fig. S2) to remove an overlapping Mn²⁺ signal. The Mn²⁺ signal is attributed to residual Mn²⁺ ions stemming from a small fraction of damaged manganese clusters. In X-band pulse EPR (not shown) and ENDOR spectra (*a*), Mn²⁺ contributions were avoided by optimizing the MW pulse lengths for the $S_2{}'$ state signal of the Mn_4O_5 spin system with an $S = 1/2$ ground spin state. Experimental parameters: *a* and *b*, MW frequencies, 9.717 GHz (X-band), 34.033 GHz (Q-band); shot repetition rate, 5 ms; MW pulse lengths π, 12 ns (X-band), 72 ns (Q-band); τ, 200 ns (X-band), 440 ns (Q-band); magnetic fields, 380 mT (X-band), 1208 mT (Q-band); RF pulse length π_{RF}, 4 μs; temperature, 5 K; *c–e*, see Refs. 45 and 49.

sensitivity Teflon membrane under continuous illumination with a tungsten lamp through an aqueous 5% $CuSO_4$ IR filter. The assay medium was the buffer of the samples lacking EDTA and with 5 mM $MgCl_2$ and 0.2 mM phenyl-*p*-benzoquinone (20 mM in dimethyl sulfoxide) added as an electron acceptor.

EPR/ENDOR Spectroscopy—X-band CW EPR spectra were recorded on a Bruker ELEXSYS E500 spectrometer equipped with an ESR900 liquid helium flow cryostat and an ITC503 helium flow temperature controller (Oxford Instruments Ltd.). X-band pulse experiments were performed with a Bruker ESP

380E spectrometer equipped with a dielectric ring resonator, an Oxford ITC liquid helium flow system, and a temperature controller. Q-band pulse experiments were performed using a Bruker ELEXSYS E580 spectrometer equipped with a laboratory-built cylindrical ENDOR resonator (58), a CF935 cryostat, and an ITC5025 temperature controller (Oxford Instruments Ltd.). Field-swept electron spin echo (ESE)-detected experiments were performed at Q-band frequencies using the pulse sequence $\pi/2$-τ- $\pi/2$-τ-echo with $\pi = 72$ ns and $\tau = 440$ ns. For ^{55}Mn Davies ENDOR, the pulse sequence was π-π_{RF}-T-$\pi/2$-τ-$\pi/2$-τ-echo, with $\pi = 12$ ns (X-band), 72 ns (Q-band), or 16 ns (Q-band Mn^{2+} titration/quantification), $\pi_{RF} = 4$ μs (X-, Q-band) or 4.5 μs (Q-band Mn^{2+} titration/quantification), $T = 3.4$ μs (X-, Q-band) or 1 μs (Q-band Mn^{2+} titration/quantification), and $\tau = 200$ ns (X-band), 440 ns (Q-Band), or 320 ns (Q-band Mn^{2+} titration/quantification). The radio frequency (RF) was varied randomly in the desired range, and the RF pulses were amplified by an ENI 5100L amplifier. Except for Mn^{2+} titration/quantification, ^{55}Mn Davies ENDOR spectra were collected using a home-built computer console with SpecMan control software (59) coupled to an SMT02 external RF pulse generator.

EPR/ENDOR Spectral Simulations—Simulations of EPR and ^{55}Mn ENDOR spectra were performed numerically using the EasySpin software package (60). The fitting procedures employed a least squares minimization routine. All tensors were set to be collinear. The Ca^{2+}-depleted Mn_4O_5 cluster in the S_2' state was treated as an effective electronic spin $S = 1/2$ ground state coupled to the four ^{55}Mn nuclei, described by the following spin Hamiltonians for the EPR (Equation 1) and ^{55}Mn ENDOR (Equation 2) spectra.

$$H_{Mn_4O_5,EPR} = \beta_e B_0 GS + \sum_{i=1}^{4}(SA_iI_i) \qquad \text{(Eq. 1)}$$

$$H_{Mn_4O_5,ENDOR} = \beta_e B_0 GS + \sum_{i=1}^{4}(\beta_n B_0 g_n I_i + SA_iI_i) \qquad \text{(Eq. 2)}$$

The EPR spectrum was calculated using second order perturbation theory, neglecting nuclear Zeeman terms and forbidden transitions. The ^{55}Mn ENDOR spectra were calculated exactly, including nuclear Zeeman terms and considering all transitions. For the monomeric Mn^{2+} ion ($S = 5/2$, $I = 5/2$) bound to the Ca^{2+}-depleted PS II, the following spin Hamiltonian was solved exactly both for the ESE and ENDOR spectra:

$$H_{Mn^{2+}} = \beta_e B_0 gS + D\left[S_z^2 - \frac{1}{3}S(S+1)\right] + E(S_x^2 - S_y^2)$$
$$+ \beta_n B_0 g_n I + SAI \qquad \text{(Eq. 3)}$$

For details on the simulation procedure and the theoretical background, see Refs. 46, 49, and 61.

Temperature-dependent CW EPR Signal Intensity—The temperature was calibrated using a thermometer in place of the sample in the EPR tube. To guarantee that the actual unsaturated intensity I_1 of the S_2' state modified multiline, as the

ground state signal, was measured at all temperatures, the saturation behavior was studied at the lowest temperature employed. As a result, the non-saturating microwave (MW) power of 0.1 milliwatt was used throughout. The intensities I_1 of the derivative signals were measured by means of the heights of 19 peaks throughout the spectral range, thereby minimizing statistical errors and contributions of underlying broader signals, such as from cytochrome b_{559} and the semiquinone-iron complex. How the ground-to-first excited state energy difference Δ is determined from the temperature dependence of I_1 is outlined in the supplemental data.

Quantification of the Relative Concentrations of PS II-bound Mn^{2+} and Hexaquo-Mn^{2+}—The Mn^{2+} species in Ca^{2+} and Mn^{2+} titration samples were quantified by means of their Q-band ^{55}Mn Davies ENDOR spectra in two ways, and the results were averaged. (i) The relative contributions of the spectra from the pure Mn^{2+} species needed to reproduce the spectra from the various titration points were determined. The spectra from Mn^{2+} already present in the Ca^{2+}-depleted PS II samples without the addition of Mn^{2+} ions and from 40 μM $MnCl_2$ dissolved in the titration buffer represented PS II-bound and hexaquo-Mn^{2+}, respectively. (ii) The relative amplitudes of the ^{55}Mn ENDOR $m_S = -3/2$ transitions, which appear in different RF ranges characteristic for the two Mn^{2+} species, were quantified in the regions of 353–376 MHz for PS II-bound Mn^{2+} and 390–395 MHz for hexaquo-Mn^{2+}.

RESULTS

EPR and ^{55}Mn ENDOR of the Ca^{2+}-depleted Mn_4O_5 Cluster in the S_2' State—The characteristic modified multiline CW EPR signal (24, 25) was observed for Ca^{2+}-depleted PS II samples poised in the S_2' state. It is centered at $g \approx 2$ and spans the magnetic field range from ~260 to ~430 mT, resolving at least 27 hyperfine interaction (HFI) lines with an average peak-to-peak spacing of ~6 mT (Fig. 2A). The central HFI lines are superimposed by the signal of the stable tyrosyl radical $Y_D^\bullet$ centered at $g \approx 2$, which is not depicted for clarity of presentation. The broad underlying signal of the reduced $Q_A^{\bar{\cdot}}$ Fe^{2+} complex (62) contributes in the 350–375-mT region (24, 25, 29).

Traces a and *b* in Fig. 2B show the X- and Q-band Davies ENDOR spectra of the S_2' state recorded at 5 K and magnetic fields of 380 and 1208 mT, respectively. The ^{55}Mn ENDOR spectrum of the Mn_4O_5 cluster in the S_2' state is essentially invariant across the corresponding EPR signal envelope (supplemental Fig. S1). It is ~130 MHz wide, extending over a range from ~60 to ~190 MHz. As compared with the ^{55}Mn ENDOR spectrum of the native S_2 state (Fig. 2Bc, supplemental Fig. S1), the Ca^{2+}-depleted S_2' state spectrum is broader. The edges of the spectrum change up to 10 MHz, resulting in a ~20 and ~10 MHz increase in the width of the X- and Q-band ^{55}Mn ENDOR spectra, respectively, as compared with the Ca^{2+}-containing S_2 state of spinach PS II (42, 45, 46). The Q-band spectrum of the S_2' state exhibits five clearly resolved peaks, as also seen for the native S_2 state spectrum from *Thermosynechococcus elongatus* (Fig. 2Bd); however, their positions differ slightly.

The X-band CW EPR and X- and Q-band ^{55}Mn Davies ENDOR spectra were simultaneously simulated using the spin Hamiltonian formalism (for details see "Experimental Proce-

TABLE 2

Isotropic and anisotropic values of the effective ^{55}Mn HFI tensors A_i ($i = 1$–4) used for the simulations of the X- and Q-band EPR and ENDOR spectra of the Ca²⁺-depleted PS II from spinach in the S_2' state (Fig. 2) and for the S_2 states of native spinach PS II (46) and native and Sr²⁺-substituted PS II from *T. elongatus* (49)

Species	OEC state	Tensor component	A_1	A_2	A_3	A_4
			MHz	*MHz*	*MHz*	*MHz*
Spinach	-Ca²⁺ S_2'	*iso*[a]	311	234	202	171
		aniso[b]	72	−84	−38	−59
	Ca²⁺ S_2	*iso*	298	248	205	193
		aniso	35	−40	−60	−70
T. elongatus	Ca²⁺ S_2	*iso*	312	251	208	191
		aniso	55	−40	−48	−108
	Sr²⁺ S_2	*iso*	332	243	203	173
		aniso	59	−37	−30	−56

[a] The isotropic $A_{i,\text{iso}}$ ($i = 1$–4) values are the averages of the principal values: $A_{i,\text{iso}} = (A_{i,x} + A_{i,y} + A_{i,z})/3$.

[b] The anisotropy in the A_i values is expressed as the difference $A_{i,\text{aniso}} = A_\perp - A_\parallel$ between the equatorial and axial components of the tensor. The equatorial and axial A_i values are defined as $A_{i,\perp} = (A_{i,x} + A_{i,y})/2$, $A_{i,\parallel} = A_{i,z}$.

dures" and Refs. 46 and 49). In these simulations, the S_2' state Mn$_4$O$_5$ cluster is treated as an effective $S = 1/2$ electronic spin state coupled to the four ^{55}Mn nuclei, the same as for the native S_2 state (41, 42, 46, 48, 49, 63–66). This approach requires the ground electronic spin state to be well separated from higher states, as is experimentally observed (see the following section). The simulations reproduce all the major spectral features of the EPR and ^{55}Mn ENDOR spectra (Fig. 2, *dashed red traces*).

The isotropic and anisotropic values of the fitted effective ^{55}Mn HFI tensors A_i ($i = 1$–4) are given in Table 2. For means of comparison, the numbers for the native S_2 state from spinach (46) and the native and Sr²⁺-substituted S_2 states from *T. elongatus* (49) are also listed. A full set of G and HFI tensor components is listed in supplemental Table S1. As seen for the Mn$_4$O$_5$Ca/Sr clusters, four effective HFI tensors are required to simulate the Mn$_4$O$_5$ cluster spectra. Their magnitudes are on the order seen for mono- and dimeric Mn³⁺ and Mn⁴⁺ complexes. Hence, their individual spin projection coefficients ρ_i must be on the order of 1 (see Ref. 49). In contrast to preliminary simulations of the S_2' spectra (67) or others on the S_2 state from spinach PS II (46), the HFI tensors were not constrained to axial symmetry. However, as was found previously in simulations of the Mn$_4$O$_5$Ca/Sr clusters in *T. elongatus* (49), the tensors nevertheless show a considerable degree of axial symmetry. Moreover, these four OEC clusters show the same geometries of their HFI tensors, with larger axial than equatorial tensor components ($A_{\text{aniso}} < 0$) for $A_2 - A_4$ and vice versa for the largest HFI A_1 ($A_{\text{aniso}} > 0$).

Spin State Energies of the Ca²⁺-depleted Mn$_4$O$_5$ Cluster in the S_2' State—The energy difference Δ of the paramagnetic ground spin state and the first exited state was estimated from the temperature dependence of the unsaturated X-band CW modified multiline signal of the Ca²⁺-depleted S_2' state. The measured intensities I_1 of the derivative signal at a series of temperatures are depicted in a Curie plot *versus* $1/T$ in Fig. 3. This relation is approximately linear over the measured range from 14.4 to 5.5 K and extrapolates to 0 for $T \rightarrow \infty$. This Curie behavior of the temperature dependence indicates that the Ca²⁺-depleted S_2' state features an $S = 1/2$ ground spin state energetically well separated from states of higher spin multiplicity. The temperature dependence of the S_2' modified multiline signal can be reproduced reasonably well with $\Delta \geq 35$ cm^{-1} corresponding to $J_{\text{eff}} \geq 12$ cm^{-1} (see "Experimental Procedures"). This relatively large separation from states of higher
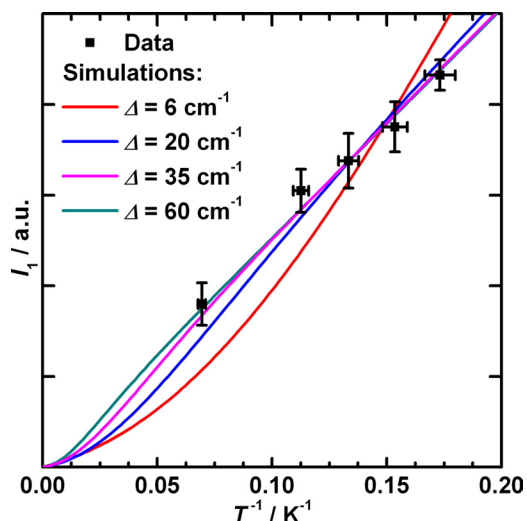

FIGURE 3. Curie plot showing the dependence of the intensity I_1 of the modified multiline derivative signal of the Ca²⁺-depleted S_2' state on the inverse temperature T. The error of the x-values comes from the calibration of the actual temperature at the sample position (see "Experimental Procedures"). The curves are simulations of the Curie temperature dependence over a range of Δ values on the basis of Equation S1 in the supplemental data and the simplified electron 2-spin coupling scheme for the OEC outlined under "Experimental Procedures." Experimental parameters: MW frequency, 9.437 GHz; MW power, 0.1 milliwatt; modulation amplitude, 0.75 mT; time constant, 82 ms; temperatures, 5.5, 6.3, 7.3, 8.7, and 14.4 K.

spin multiplicity allows the S_2' state Mn$_4$O$_5$ spin system to be treated in the strong exchange limit, *i.e.* as an effective $S = 1/2$ spin state, as assumed in the previous section.

EPR and ^{55}Mn ENDOR of a Specifically Bound Mn²⁺ Ion—The Ca²⁺-depleted PS II preparations exhibit an additional EPR and ENDOR signal in all accessible S' states that is not present in native PS II samples. At 5 K, Q-band ESE-detected field sweep EPR spectra of the dark-adapted Ca²⁺-depleted PS II preparations (S_1' state), in which the Mn$_4$O$_5$ cluster does not show a perpendicular mode EPR signal, displayed a broad EPR signal centered at $g = 1.99$ with a full width at half-maximum of ~63 mT (Fig. 4, *inset*). A corresponding signal was not observed using CW X-band EPR spectroscopy; the signal is probably too broad to be discerned from the base-line drift in the CW EPR experiment (51). Q-band Davies ENDOR spectra were recorded at several magnetic fields in the RF frequency range of 30 to 400 MHz (Fig. 4). The ^{55}Mn ENDOR spectra are dominated by two broad peaks between 100–195 MHz and another line centered at ~370 MHz. The two lines at 100–195 MHz are
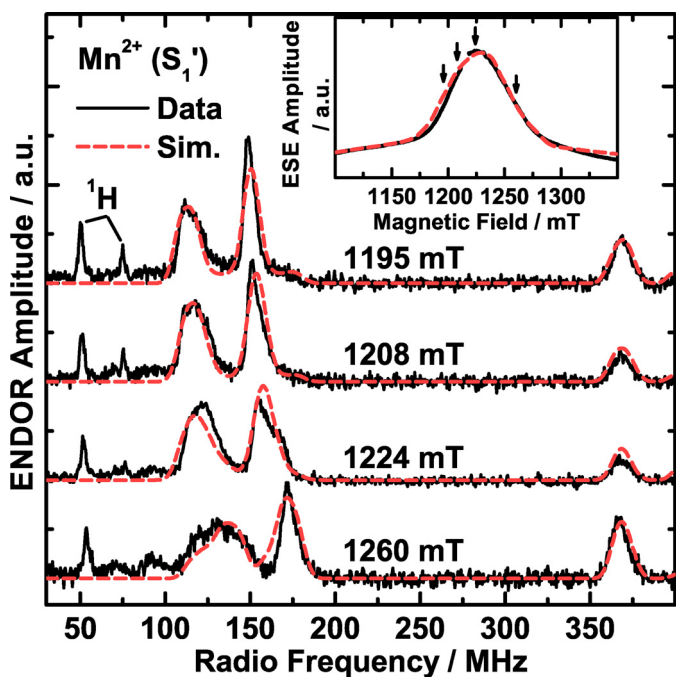
FIGURE 4. **Q-band pulse ESE-detected field-swept EPR (*inset*) and Davies ENDOR experimental spectra (*black solid traces*) and simulations (*Sim.; red dashed traces*) of the Mn²⁺ ion bound to Ca²⁺-depleted PS II isolated from spinach and poised in the S₁′ state.** In the EPR spectrum, the region of the overlapping $Y_D^\bullet$ EPR signal ($g \approx 2$) is not displayed for clarity and was omitted in the simulations. The *arrows* indicate the four magnetic fields at which the ENDOR spectra were measured. Experimental parameters: MW frequency, 34.07 GHz; shot repetition rate, 5 ms; MW pulse length π, 72 ns; τ, 440 ns; Davies ENDOR, magnetic fields, 1195, 1208, 1224, 1260 mT (*top to bottom*); RF pulse length π_{RF}, 4 µs; temperature, 5 K.

dependent on the magnetic field and shift to higher frequencies with increasing magnetic field. The spectra also contain sharp proton signals, one centered at the ¹H Larmor frequency (~50 MHz) and a strongly coupled one at ~75 MHz with decreasing amplitude at increasing field positions. Its partner at low frequency (~25 MHz) lies outside the spectral range. No further low frequency signals were detected for this species using either ENDOR or electron spin echo envelope modulation (ESEEM).

These EPR and ⁵⁵Mn ENDOR signals can be readily assigned to high spin Mn²⁺ with $S = 5/2$, although their appearance is different from the spectra typically associated with Mn²⁺ complexes (see Discussion and Fig. 5A). Simultaneous simulations of the EPR and of four ENDOR spectra at different magnetic fields (Fig. 4, *dashed red traces*) are consistent with this assignment. They reproduce both the spectral breadth and line shape of the EPR absorption signal and the peaks in the four ⁵⁵Mn ENDOR spectra. Besides a near-isotropic G tensor (principal values 1.983, 1.996, 2.002), the simulations yielded an almost isotropic HFI tensor with the principal components $A_x = 256$ MHz, $A_y = 260$ MHz and $A_z = 257$ MHz, resulting in an isotropic average A_{iso} of 258 MHz. In addition, the simulations required a large fine structure parameter $D = -2355$ MHz with a pronounced rhombicity $\eta = E/D = -0.38$ of the zero-field splitting (ZFS). It is noted that the predominant contribution to the width of the EPR and ENDOR signals is the large and rhombic ZFS interaction (more information on the effect of the ZFS can be found in the supplemental data and Ref. 61). Hence, considering the good agreement of the measured and calcu-
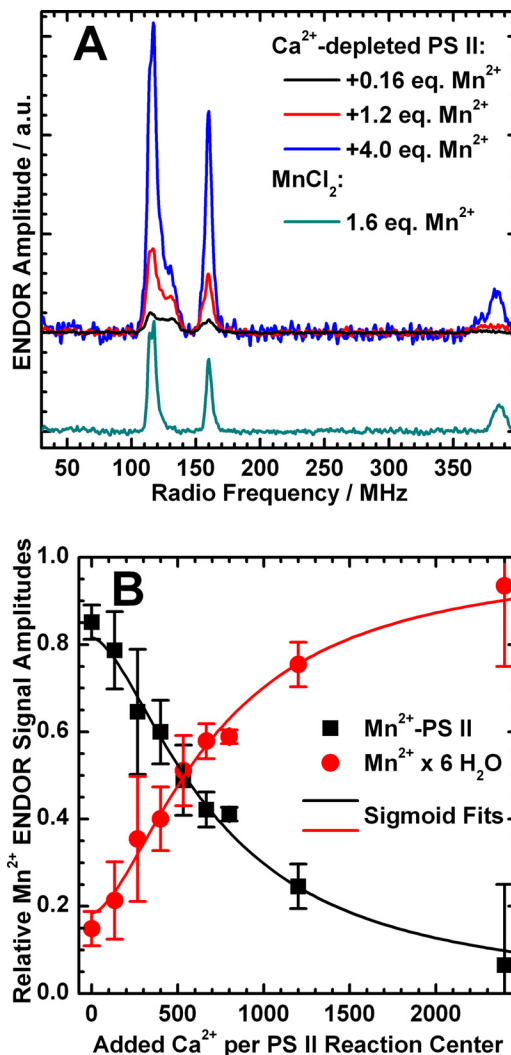

FIGURE 5. **Mn²⁺ and Ca²⁺ titrations monitored by Q-band ⁵⁵Mn ENDOR.** *A*, Q-band ⁵⁵Mn Davies ENDOR spectra of dark-adapted Ca²⁺-depleted PS II samples (S₁′ state) with 0.16, 1.2, and 4.0 eq (*black*, *red*, and *blue trace*) of Mn²⁺ ions added relative to the number of PS II RCs and of 40 µM MnCl₂ (corresponding to 1.6 eq) dissolved in the same buffer used for the PS II titration experiments. For the titration curve, see supplemental Fig. S3. The spectra were smoothed using a 5-point moving average. *B*, titration of Ca²⁺-depleted PS II samples containing 1 eq of Mn²⁺ ions with respect to the PS II RCs with Ca²⁺. The relative ⁵⁵Mn ENDOR signal amplitudes of Mn²⁺ ions bound to the PS II protein complex (*black squares*) and hexaquo-Mn²⁺ in solution (*red circles*), quantified as described under "Experimental Procedures," are plotted against the equivalents of Ca²⁺ ions added to the samples. The concentrations of both Mn²⁺ species as a function of added Ca²⁺ were reproduced by a sigmoid fit curve (*solid lines*). The concentration of RCs in the samples was 25 ± 3 µM. Experimental parameters: MW frequency, 34.03 GHz; shot repetition rate, 5 ms; MW pulse length π, 16 ns; τ, 320 ns; magnetic field, 1224 mT; RF pulse length π_{RF}, 4.5 µs; temperature, 5 K.

lated EPR and ENDOR signals (Fig. 4), the optimized fine structure parameter D can be considered robust; *i.e.* a single set of D and E values is sufficient to rationalize the data. The fact that the inclusion of a distribution of the ZFS parameters is not required indicates that there are only small site-to-site inhomogeneities of the Mn²⁺ ligand sphere. Therefore, we propose that the Mn²⁺ ion is bound to one specific site in Ca²⁺-depleted PS II.

Mn²⁺ and Ca²⁺ Titration Experiments—To further investigate the Mn²⁺ species described in the previous section, Mn²⁺ and Ca²⁺ titration experiments of Ca²⁺-depleted PS II samples

were performed, monitoring the CW EPR and ENDOR signal described above.

Mn^{2+}/Ca^{2+} Titration Monitored by CW EPR—Mn^{2+} ions were added to Ca^{2+}-depleted PS II samples and the characteristic S$_2'$Y$_Z^\bullet$ state split signal, S$_2'$ multiline signal, and hexaquo-Mn^{2+} signal (not shown) were measured. The addition of ≤0.8 eq of Mn^{2+} ions relative to the number of PS II RCs did not quantitatively alter the three signals. The Mn^{2+} ions added are CW EPR-silent, as seen in the study of Booth *et al.* (51), which is consistent with a protein-bound Mn^{2+} species. In addition, this species does not cause any line broadening or even splitting of the signals from the OEC or the tyrosyl radicals. The addition of ≥0.8 equivalents of Mn^{2+} ions resulted in the appearance of the hexaquo-Mn^{2+} signal. The subsequent addition of Ca^{2+} to Ca^{2+}-depleted, Mn^{2+}-loaded PS II samples led to a loss of the S$_2'$Y$_Z^\bullet$ state split signal and of the multiline signal, as the Ca^{2+}-reconstituted Mn$_4$O$_5$Ca cluster can proceed beyond the S$_2'$ state upon illumination. A concomitant increase of the Mn^{2+} six-line signal was observed due to the release of the PS II-bound Mn^{2+} into solution (51).

Mn^{2+}/Ca^{2+} Titration Monitored by ^{55}Mn ENDOR—Mn^{2+} binding was also directly monitored by Q-band ENDOR. The concentrations of PS II-bound and solubilized Mn^{2+} ions in each sample were quantified by means of the relative amplitudes of their characteristic ^{55}Mn ENDOR signals (Fig. 5*A*; for the titration curve, see supplemental Fig. S3). Without the addition of MnCl$_2$, dark-adapted Ca^{2+}-depleted PS II (S$_1'$ state) always displayed the PS II-bound Mn^{2+} signal shown in Fig. 4. The addition of ~0.8 eq of MnCl$_2$ led to a 4–5-fold increase of this signal with only little free hexaquo-Mn^{2+} (15 ± 4%) present at the same time. This suggests that ~20% of RCs contain a bound Mn^{2+} before exogenous addition of MnCl$_2$ so that in the end a total of ~1 eq Mn^{2+} is in the sample. The basal Mn^{2+} is likely derived from centers damaged during the Ca^{2+} depletion procedure and nominally corresponds to the loss of ~5% Mn$_4$O$_5$(Ca) clusters. The high occupancy of the Mn^{2+} site suggests that it is of high affinity, with a dissociation constant K_D that is too small to be determined here. From the employed concentrations of the binding partner, K_D is expected to be in the submicromolar/nanomolar range. It is also noted that the addition of the chelating agent EDTA did not remove or alter the appearance of the bound Mn^{2+} signal, consistent with the protein site having a high affinity for Mn^{2+}.

An additional Ca^{2+} titration was performed on the fully Mn^{2+}-loaded Ca^{2+}-depleted PS II (+0.8 eq of MnCl$_2$, *i.e.* a final ratio of 1 Mn^{2+} ion per PS II RC). The Ca^{2+} concentrations ranged from 0 to 2400 eq Ca^{2+} per RC (0–60 mM). In Fig. 5*B*, the relative concentrations of the two Mn^{2+} species (PS II-bound and solubilized) are plotted against the equivalents of Ca^{2+} ions added. This behavior could be reproduced by a sigmoid curve with a half-saturation value of 700 Ca^{2+} ions per RC. This value is similar to 1200 eq of Ca^{2+} reported in Booth *et al.* (51). The difference may be due to the Ca^{2+} depletion method used, the low pH/citrate treatment in this study *versus* a NaCl salt wash (24) in the study of Booth *et al.* (51). Their differing effects on the extrinsic PS II subunit composition could alter the Ca^{2+} binding kinetics (see Refs. 24 and 51).

DISCUSSION

Location of the Mn^{2+} Binding Site—Based on the observations described above (see "Results"), a preliminary assignment can be made as to where the binding site of the Mn^{2+} ion is located. No strong magnetic interaction was observed between the Mn^{2+} ion and the Ca^{2+}-depleted Mn$_4$O$_5$ cluster or the tyrosyl radical Y$_Z^\bullet$ in the form of a broadening or splitting of the corresponding EPR signals. Thus, Mn^{2+} binding directly to the Ca^{2+} site of the OEC can be excluded. This Mn^{2+} ion must be at least 10 Å away not to be detectable via dipolar magnetic interaction. A similar argument holds for Y$_D^\bullet$ (D2-Tyr-160), as it also displays an unperturbed EPR lineshape when Mn^{2+} is bound. These "exclusion zones" are indicated by *green* and *violet spheres* in Fig. 6*A*. There is, however, a long range dipolar interaction between the Mn^{2+} ion and Y$_D^\bullet$ as evidenced by the relaxation enhancement of its EPR signal (51). Being smaller than the enhancement resulting from the Mn$_4$O$_5$Ca cluster in the S$_2$ state suggests a weaker Mn^{2+}-Y$_D^\bullet$ interaction and thus a longer distance than the 31 Å measured between the cluster and Y$_D$ (6).

The binding and titration behavior can either be rationalized by a significant allosteric effect of Ca^{2+} on the Mn^{2+} site, or Mn^{2+} binding could take place directly at a depleted Ca^{2+} site. The recent crystal structure (6) of PS II from *Thermosynechococcus vulcanus* exhibits three additional Ca^{2+} sites at distances greater than 30 Å from the paramagnetic species monitored, *i.e.* the Mn$_4$O$_5$(Ca) cluster, Y$_Z^\bullet$, and Y$_D^\bullet$ (Fig. 6*A*). In the structure of PS II from *T. elongatus*, a different Ca^{2+} site in PsbO has been identified (4, 5, 68), not found in the *T. vulcanus* crystals. All these Ca^{2+} sites are located on the lumenal/donor side of PS II in the subunit CP47, the cytochrome b_{559} subunit β (PsbF), and the extrinsic protein PsbO, and are solvent-accessible. It is not clear, however, whether Ca^{2+} binding at these sites is solely a crystallization artifact under the conditions used or of physiological relevance. With the exception of the two sites in PsbO, the Ca^{2+} sites appear to be of low affinity, as the Ca^{2+} ions are ligated to a large part by H$_2$O and glycerol. In contrast, the two Ca^{2+} sites seen in the PsbO possess at least three ligands from amino acid side chains (Fig. 6, *B* and *C*) and thus are potentially of high affinity. In the homologous PsbO from spinach, which has also been reported to bind Ca^{2+} (69–71), Asn-197 and Val-198 of the binding motif in Fig. 6*B* correspond to the conserved residues Ser-286 and Val-287, whereas there is no equivalent for Thr-135. Glu-81, Glu-140, and His-257 in the other binding motif (Fig. 6*C*) correspond to Glu-146, Glu-205, and Glu-317 (for a sequence alignment, see supplemental Fig. S4). Mn^{2+} binding to PsbO has indeed been demonstrated previously in isolated PsbO from higher plants (72–74). As in the present study and Ref. 51, protein-bound Mn^{2+} did not show a CW EPR signal, but a six-line signal was observed after denaturation of the protein (73). PsbO was reported to show carbonic anhydrase activity, which was maximal in the presence of Mn^{2+} (74).

The magnetic properties of the Mn^{2+} ion provide information about the immediate ligand environment in this binding pocket. The D and E values of Mn^{2+} complexes of higher symmetry, such as Mn^{2+}-EDTA and hexaquo-Mn^{2+}, are significantly smaller than those for the PS II-bound Mn^{2+} described
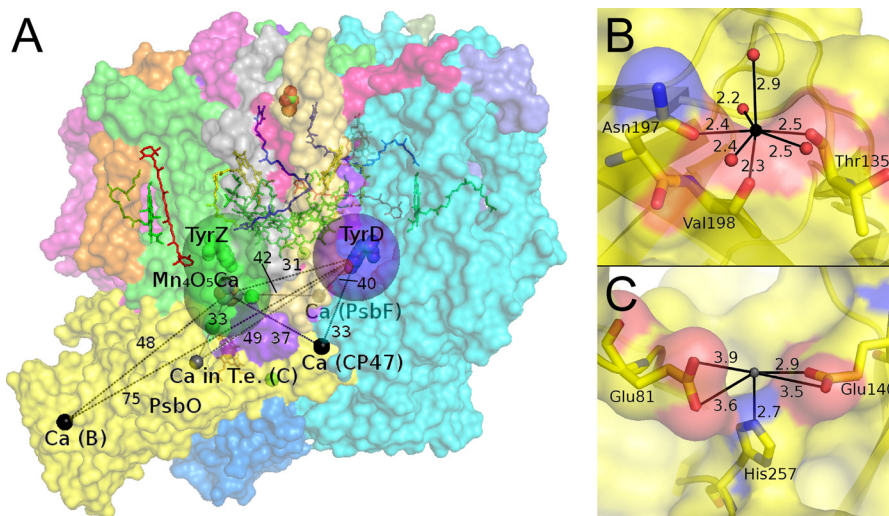
Electronic Structure of the Ca²⁺-depleted OEC of Photosystem II

FIGURE 6. **Ca²⁺ and potential Mn²⁺ binding sites in cyanobacterial PS II crystals.** *A*, PS II crystal structure from *T. vulcanus* (6) (PDB accession number 3ARC) highlighting the Ca²⁺ ions (*black spheres*) as well as a Ca²⁺ binding site found in PS II from *T. elongatus* (*gray sphere*) and their distances to the paramagnetic entities Mn_4O_5Ca cluster, Y_Z·, and Y_D·. The 10 Å spheres around the latter indicate the approximate region in which a bound Mn²⁺ would cause a splitting of their EPR signals and thus can be excluded to contain the Mn²⁺ binding site. *B* and *C*, ligand environments of the Ca²⁺ ions in the extrinsic PsbO proteins from *T. vulcanus* and *T. elongatus* (*T.e.*) (5), respectively. Oxygen, nitrogen, and carbon atoms are shown in *red*, *blue*, and *yellow*, respectively. Differences between the PsbO proteins of these cyanobacterial species and from higher plant spinach are displayed by a sequence alignment in supplemental Fig. S4. All distances are in Å.

here (see supplemental data and Ref. 61). The large and highly rhombic ZFS reflects an asymmetric coordination sphere. Both the 7- and the 5-fold coordination geometries of the Ca²⁺ ions in PsbO from the two cyanobacterial species exhibit considerable asymmetry (Fig. 6, *B* and *C*). In addition, the large proton coupling seen also suggests the Mn²⁺ ion to have at least one water ligand. The absence of any smaller coupling, such as from ¹⁴N (not shown), indicates that the Mn²⁺ ion does not bind to a N-containing ligand residue like histidine. Thus, the absence of a (visible) water and the presence of His-257 as ligands of the Ca²⁺ ion in *T. elongatus* PsbO (Fig. 6C) favor Mn²⁺ binding to the Ca²⁺ site in PsbO identified in the *T. vulcanus* crystal structure (Fig. 6B).

PS II from higher plants exhibits an extrinsic subunit composition different from that of the cyanobacterial system. Higher plant lumenal PsbP has been reported to be capable of binding Mn²⁺ stoichiometrically (75, 76). Similar to Ca²⁺-depleted PS II in this study and in Ref. 51, isolated PsbP loaded with Mn²⁺ did not show a Mn²⁺ X-band CW EPR signal unless it was denatured. A bound Mn²⁺ could be detected by high field EPR spectroscopy and distinguished from non-specifically attached Mn²⁺, similar to the present study. It is noted though that the binding constant reported in Bondarava *et al.* (76) is probably incorrect; for a discussion, see Ref. 77. Moreover, the Mn²⁺ ion in PsbP could be (partially) replaced by Ca²⁺, and Zn²⁺ has been found to bind at one of the two proposed Mn²⁺ sites in PsbP crystals from spinach (PDB accession number 2VU4) and its cyanobacterial homologue CyanoP (78). Mn²⁺ bound to the PsbP would be at least 30 Å from either the OEC or Y_D, again consistent with the distance constraints identified above. Thus, PsbP could also contain the putative site of specific Mn²⁺ binding in Ca²⁺-depleted higher plant PS II.

The physiological role of the putative Mn²⁺ binding site is the delivery of Mn²⁺ to the OEC during photoassembly and/or the storage of Mn²⁺ during the damage/repair cycle of the D1

protein (see Refs. 79–82). Ca²⁺ is essential for photoactivation of the OEC. It was suggested to bind at a site within the PS II complex, which leads to a conformational change of the protein pocket where the OEC is assembled (*i.e.* the C terminus of D1). Thus, it appears reasonable that in the absence of Ca²⁺, it is favorable for the PS II supercomplex to sequester in a site Mn²⁺ that can be rapidly delivered upon an increase in Ca²⁺ concentration. In this scenario the lumenal Ca²⁺ concentration would be a signaling mechanism for OEC assembly and repair.

Spectral Properties of the Mn_4O_5 Cluster in the S_2' State Compared with Other S_2 State Systems—The appearance of the ⁵⁵Mn ENDOR spectra, the fitted ⁵⁵Mn HFI tensors, and the ground-to-first excited state energy separation of the Ca²⁺-depleted S_2' state all fall within the natural spectral variations observed for the native S_2 states in different species (41). This demonstrates that the basic electronic and thus also spatial structure of the Mn_4O_5 cluster remains intact upon Ca²⁺ removal. This confirms and further refines observations on the interatomic distances of the manganese ions from earlier EXAFS experiments (29).

The Ca²⁺-depleted S_2' state from spinach resembles the native S_2 state from *T. elongatus* with regard to the spin state energies. Upon removal of the Ca²⁺ ion, Δ increases to ≥35 cm⁻¹, which is much larger than for the native spinach S_2 state (Δ = 3–6 cm⁻¹) but more similar to *T. elongatus* (Δ = 12–25 cm⁻¹) (41, 83, 84). In intact spinach PS II, the energy ladder is sensitive to MeOH addition. The mechanism by which MeOH binding perturbs the electronic structure of the S_2 state was recently discussed in Su *et al.* (41). In the model proposed, MeOH binding to the OEC increases the electronic coupling of the pending manganese (Mn_{A4}) to the cuboidal (Mn_{B3}, Mn_{C2}, Mn_{D1}) unit. It is this effective coupling that defines the ground-to-first excited state energy difference Δ of the S_2 state. Ca²⁺ depletion appears to have the same effect. However, the addition of MeOH did not modify the appearance of the S_2' state
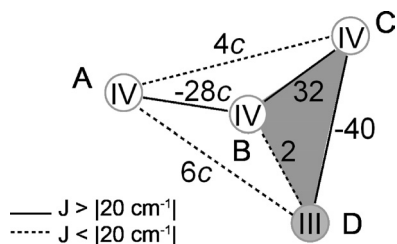
FIGURE 7. Model for the electronic structure of the OEC in the native S$_2$ and Ca^{2+}-depleted S$_2'$ states calculated based on a refined DFT structure of the OEC (18) in the latest crystal structure (6). *A–D* label the manganese ions in their respective oxidation state, and the numbers give the pair-wise exchange coupling J_{ij} between the electronic spins of the Mn^{III} and Mn^{IV} ions in cm^{-1}. The constant c is 1 in the originally derived model but differs for the various clusters and conditions, such as the presence or absence of MeOH. The S$_2'$ state can be described by the scheme with $c = 1.65$.

TABLE 3

Calculated spin projection tensor components $\rho_\perp$ and $\rho_\parallel$, intrinsic ^{55}Mn HFI tensor components $a_\perp$ and $a_\parallel$ and isotropic and anisotropic intrinsic HFI values a_{iso} and a_{aniso} for the Mn ions of the OEC in the Ca^{2+}-depleted S$_2'$ state on the basis of the electronic exchange coupling scheme in Fig. 7 with $c = 1.65$ and intrinsic ZFS values $d_{A4} = d_{B3} = d_{C2} = 0$ cm^{-1} for the Mn^{IV} ions and $d_{D1} = -2.27$ cm^{-1} for the Mn$_{D1}^{III}$ ion

Manganese ion	$\rho_\perp$	$\rho_\parallel$	$a_\perp{}^a$	$a_\parallel{}^a$	$a_{iso}{}^b$	$a_{aniso}{}^c$
			MHz	*MHz*	*MHz*	*MHz*
Mn$_{A4}$ (Mn^{IV})	1.03	1.25	197	230	208	33
Mn$_{B3}$ (Mn^{IV})	−0.81	−1.09	187	190	188	3
Mn$_{C2}$ (Mn^{IV})	−0.87	−1.21	220	188	209	−31
Mn$_{D1}$ (Mn^{III})	1.66	2.04	202	123	175	−79

^{a} The equatorial and axial a_i values are defined as: $a_\perp = (a_x + a_y)/2$, $a_\parallel = a_z$.
^{b} The isotropic a_{iso} values are the averages of the individual components of the tensor $a_{iso} = (a_x + a_y + a_z)/3$.
^{c} The anisotropy of the a tensor is expressed as the difference $a_{aniso} = a_\parallel - a_\perp$ between the parallel and perpendicular tensor components.

ESE and ENDOR spectra (not shown). It is emphasized though that this effect is of the same size as that of the variation between species and thus is unlikely to be of physiological significance.

Electronic Structure/Exchange Coupling Scheme of the Ca^{2+}-depleted Mn$_4$O$_5$ Cluster in the S$_2'$ State—To further rationalize the spectral results from the Ca^{2+}-depleted Mn$_4$O$_5$ cluster, a spin coupling scheme for the S$_2'$ state was developed. It was constructed to meet the following requirements: (i) a ground state of spin multiplicity $S = 1/2$, (ii) a ground-to-first excited state energy difference $\Delta \approx 35$ cm^{-1}, (iii) spin projection factors $|\rho_i| \approx 1$ for all four manganese electronic spins, and (iv) intrinsic ZFS constants d_i of the manganese ions that lie within the range found for mono- and dimeric model complexes, *i.e.* 1 cm^{-1} < $|d|$ < 5 cm^{-1} for Mn^{III} and $|d|$ < 0.1 cm^{-1} for Mn^{IV} ions in an octahedral ligand environment (see Refs. 18, 47, and 49). The inferred structural (29) and spectral similarity of the native and the Ca^{2+}-depleted manganese cluster suggest that the spin coupling scheme for the native S$_2$ state (Fig. 7, $c = 1$) (18), in which Mn$_{D1}$ is the Mn^{III} ion, can be used as a starting point. Calculated on the basis of the refined model of the OEC in the latest crystal structure (6), the basic arrangement of this scheme is in accordance with the spatial organization as described by Siegbahn and our group (17, 18, 47, 85), in which Mn$_{B3}$, Mn$_{C2}$, and Mn$_{D1}$ form a trimeric core unit connected to Mn$_{A4}$ by a di-μ-oxo bridge via Mn$_{B3}$ (Fig. 1). Thus, this scheme represents an extension of the (3 + 1)- or Y-coupling schemes, proposed earlier in EPR spectroscopic studies (42, 46, 47, 49), where $J_{A4-C2} = J_{A4-D1} = 0$.

The coupling topology fulfills criteria (i) and (iii) as ground spin state multiplicity and spin projection factors are the same for the two states, S$_2$ and S$_2'$. In contrast, their ground-to-first excited state energy differences Δ and effective ^{55}Mn HFI tensors A_i, relevant for (ii) and (iv), are different. Thus, the $\Delta = 10.5$ cm^{-1} calculated for the S$_2$ state coupling scheme also differs from the experimental $\Delta \geq 35$ cm^{-1} determined for the S$_2'$ state. Correlations between the exchange coupling scheme and this energy difference have been investigated in previous studies (41, 47). One mechanism by which Δ is influenced directly was shown to be the strength and the sign of the exchange coupling between Mn$_{A4}$ and the trimeric unit comprising Mn$_{B3}$, Mn$_{C2}$, and Mn$_{D1}$. An increase or decrease in the magnitudes of the coupling constant J_{A4-B3} results in a larger or

smaller energy gap, respectively. As the monomer-trimer joint is in the vicinity of a possible binding site of a MeOH molecule, this rationalizes the effect of MeOH on the electronic structure of the Mn$_4$O$_5$Ca cluster in the native S$_2$ state (41). For the Ca^{2+}-depleted S$_2'$ state, the coupling of Mn$_{A4}$ to the trimeric unit was varied by multiplying the respective exchange coupling constants J_{A4-B3}, J_{A4-C2}, and J_{A4-C2} by a factor c (Fig. 7). It can be readily calculated that with $c = 1.65$ ($J_{A4-B3} = -46$ cm^{-1}, $J_{A4-C2} = 7$ cm^{-1}, and $J_{A4-D1} = 10$ cm^{-1}), Δ is 35 cm^{-1} and thus in the desired range.

For testing whether the obtained model also reproduces reasonable estimates for the intrinsic ZFS values d_i of the Mn^{III} and Mn^{IV} ions, a brief description on how those can be assessed based on the inferred coupling scheme and the fitted effective HFI tensors is given in the supplemental data. Because of their inherently small ZFSs, the d_i values of the three Mn^{IV} ions can be assumed to be 0 cm^{-1} for the calculations of the intrinsic HFI tensors a_i from the fitted effective A_i and the computed ρ_i tensors. Mn^{III} ions generally exhibit an absolute isotropic HFI value $|a_{iso}|$ in the range between 165 and 225 MHz and considerable anisotropy defined as the difference $a_{i,aniso} = |a_\parallel| - |a_\perp|$ between the absolute values. Mn^{IV} ions tend to exhibit slightly larger isotropic HFI values ($|a_{iso}| = 187$–253 MHz) and only small intrinsic HFI anisotropies ($|a_{iso}|$ < ~30 MHz) (see Ref. 49). For the Ca^{2+}-depleted S$_2'$ state, a ZFS value d_{D1} of the Mn$_{D1}^{III}$ ion in the range of −2.24 to −2.31 cm^{-1} yields a_i tensors consistent with the valence states of the individual manganese ions. An optimized ZFS value $d_{D1} = -2.27$ cm^{-1} leads to the spin projection and intrinsic HFI tensors ρ_i and a_i listed in Table 3. In terms of the intrinsic isotropic and anisotropic HFI values, the calculated numbers match the prerequisites as found in the literature very well. As the ZFS $d_{D1} = -2.24$ to −2.31 cm^{-1} lies in the range usually found for Mn^{III} ions (1 cm^{-1} < $|d|$ < 5 cm^{-1}), the developed model fulfills the four essential criteria imposed.

Structural Implications of the Zero-field Splitting d_{D1} of the Mn$_{D1}^{III}$ Ion—The removal of the Ca^{2+} ion from the spinach OEC is found to result in a significant change of d_{D1} from −1.2 cm^{-1} (41) to −2.2 to −2.3 cm^{-1}. This perturbation is larger than for the Ca^{2+}/Sr^{2+} replacement in PS II from *T. elongatus*. For these systems, the intrinsic ZFS values of the Mn$_{D1}^{III}$ ion are relatively similar (Ca^{2+}, $d_{D1} = -1.3$ cm^{-1}; Sr^{2+}, $d_{D1} =$

Electronic Structure of the Ca^{2+}-depleted OEC of Photosystem II
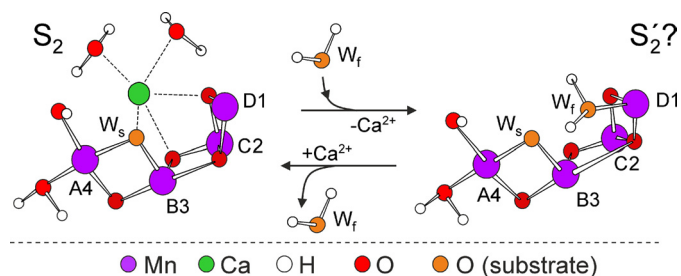

FIGURE 8. **Scheme of the native Mn$_4$O$_5$Ca cluster in the S$_2$ state and the Ca^{2+}-depleted S$_2'$ state represented by a hypothesized Mn$_4$O$_5$ cluster.** In the putative S$_2'$ state, the fast exchanging substrate water is already bound to Mn$_{D1}^{III}$, filling the space of the Ca^{2+} ion. W_s and W_f denote the slowly and fast exchanging substrate waters, respectively (96, 99).

-1.2 cm^{-1}) (49). It is, however, noted that the signs of the d_{D1} and of the HFI anisotropy of the Mn^{III} ion do not change between the Ca^{2+}-depleted S$_2'$ and the Ca^{2+}-containing S$_2$ state. These parameters can be related to the ligand sphere of the Mn^{III} ion (86–88). Negative numbers for d_{D1} and $a_{D1,aniso}$ correspond to a $^5B_{1g}$ ground state, obtained in the cases of square pyramidal 5-coordinate or tetragonally elongated 6-coordinate ligand geometries. This suggests the coordination sphere of the Mn$_{D1}^{III}$ for the S$_2'$ and S$_2$ states to be similar. However, the increase in the magnitude of d_{D1} upon Ca^{2+} removal does indicate modifications of the precise binding mode, *e.g.* altered ligand distances and angles. One possible mechanism for altering d_{D1} is protonation of one of the μ-oxo bridges ligating the Ca^{2+} ion (Fig. 1) as a means of overall charge compensation of the cluster upon Ca^{2+} removal. It is known from model complexes that Mn-Mn distances are elongated upon protonation of Mn-O-Mn bridges (89). However, within the trimeric cuboidal unit, this lengthening could be strongly impaired for the Mn$_{C2}$-Mn$_{D1}$ distance. The fitted averaged distance of the Mn-Mn interactions at 2.7–2.8 Å from EXAFS on Ca^{2+}-depleted PS II samples (29), however, does not allow for a conclusive assessment. Also, glutamate 189 of the D1 protein (D1-Glu-189), which directly coordinates the Mn$_{D1}^{III}$ (6, 17, 47) and potentially also the Ca^{2+} ion (18), could be reoriented upon Ca^{2+} depletion leading to a distortion of the coordination sphere and thus an altered d_{D1}.

In the latest crystal structure, all four manganese ions are 6-coordinate (6). This, however, requires the O5 μ-oxo bridge to be a ligand of Mn$_{A4}$, Mn$_{B3}$, and Mn$_{D1}$, engendering very long Mn-O5 bond distances well outside the range seen in model complexes (see Ref. 18) and by EXAFS spectroscopy of the Mn$_4$O$_5$Ca cluster in PS II (90, 91). In most geometry-optimized DFT structures, such as those proposed by Siegbahn and our group (17, 18, 47), the position of O5 is significantly altered (Fig. 1). The O5 shifts toward the Mn$_{A4}$, forming a genuine μ-oxo bridge between Mn$_{A4}$ and Mn$_{B3}$, and results in Mn$_{D1}$ having an open coordination site. In this case, in the Ca^{2+}-depleted S$_2'$ state, Glu-189 might function as a bidentate ligand in a then tetragonally elongated 6-coordinate Mn$_{D1}^{III}$ ligand sphere, leading to the observed change of d_{D1}.

Alternatively, the absence of Ca^{2+} may allow this open site to be occupied by a water molecule in the S$_2'$ state (Fig. 8) forming a sixth ligand to Mn$_{D1}$. The Mn$_{D1}$-bound water molecule is the second substrate water in the mechanism proposed by Siegbahn (17), which potentially binds during the S$_2$-to-S$_3$ transition. Thus, within this model, one of the roles of Ca^{2+} in the active cluster would be to prevent the second substrate from binding too early in the reaction cycle (25, 92). This activity would presumably avoid detrimental side product formation (reactive oxygen species) and lead to single product (O$_2$) formation. Consistent with this role for the Ca^{2+} ion is the known S state dependence of the affinity of Ca^{2+} to this site (93). It drops significantly in the S$_3$ state, suggesting that in this state Ca^{2+} is less tightly bound, having a more flexible ligand sphere that potentially allows greater solvent access to the Mn$_{D1}$ ion.

Besides μ-oxo bridge protonation, the loss of two positive charges is likely to be compensated by protonation of amino acid residues ligating the Ca^{2+} ion in the intact cluster. Other possibilities are the replacement of Ca^{2+} by monovalent Na$^+$ in the samples or the absence of complete charge compensation, leaving the Mn$_4$O$_5$ cluster with an additional negative charge. It is evident that any of these modifications could have a critical effect on the catalytic capabilities of the cluster, especially with regard to proton-coupled electron transfer to Y$_Z$. In light of the proposed deprotonation sequence 1,0,1,2 for the individual oxidation steps starting from S$_0$ (94), this would explain the Mn$_4$O$_5$ cluster being able to advance to S$_2'$ but not from S$_2'$Y$_Z^\bullet$ to S$_3'$.

Conclusions—This study demonstrates that Ca^{2+} is not required for conferring the critical electronic properties to the Mn$_4$O$_5$Ca cluster. This also confirms that Ca^{2+} is not essential for structural maintenance of the OEC. Its presence or absence does not affect the position of the only Mn^{III} ion of the cluster in the S$_2$/S$_2'$ state (Mn$_{D1}$), and the contribution of the four manganese ions to the electronic states S$_2$ and S$_2'$ does not differ considerably. Thus, the necessity for Ca^{2+} in water splitting catalysis must be due to another functional role of the Ca^{2+} ion.

Although the exact mechanism of inhibition upon Ca^{2+} removal is still unclear, two models can be considered in terms of the two basic catalytic mechanisms proposed in the literature. (i) For mechanisms that involve O-O bond formation between a Ca^{2+}-bound and a manganese-bound substrate water (be it a terminal ligand Mn^V = O or a μ-oxo bridge) (11, 95–97), inhibition due to Ca^{2+} depletion is readily explained. The enzyme is inactive, as it has lost a substrate binding site. It should be noted though that this model provides no rationale for the fact that the catalytic cycle is blocked at the stage of S$_2'$Y$_Z^\bullet$. (ii) Instead, O-O bond formation has been proposed to follow a mechanism that results in the coupling of substrates bound to two manganese sites (be it between two terminal bound Mn-O ligands or involving a μ-oxo bridge via oxyl radical coupling) (10, 14, 16, 17, 98). Then, inhibition due to Ca^{2+} removal probably represents a secondary effect where the Ca^{2+} ion is critical for maintaining the H-bond network between Y$_Z$ and the manganese cluster (6, 11, 30) as opposed (or in addition) to perturbation of substrate binding. Thus, Ca^{2+} removal would disable proton-coupled electron transfer during the S$_2'$Y$_Z^\bullet$-to-S$_3'$ transition, preventing substrate deprotonation and concomitant oxidation of Mn$_{D1}^{III}$. Therefore, the elucidation of the mechanistic role of the Ca^{2+} ion in the OEC is tightly linked to understanding the mechanism of photosynthetic water splitting.

REFERENCES

1. Zouni, A., Witt, H. T., Kern, J., Fromme, P., Krauss, N., Saenger, W., and Orth, P. (2001) Crystal structure of photosystem II from *Synechococcus elongatus* at 3.8 Å resolution. *Nature* **409,** 739–743

2. Kamiya, N., and Shen, J. R. (2003) Crystal structure of oxygen-evolving photosystem II from *Thermosynechococcus vulcanus* at 3.7 Å resolution. *Proc. Natl. Acad. Sci. U.S.A.* **100,** 98–103

3. Ferreira, K. N., Iverson, T. M., Maghlaoui, K., Barber, J., and Iwata, S. (2004) Architecture of the photosynthetic oxygen-evolving center. *Science* **303,** 1831–1838

4. Loll, B., Kern, J., Saenger, W., Zouni, A., and Biesiadka, J. (2005) Toward complete cofactor arrangement in the 3.0 Å resolution structure of photosystem II. *Nature* **438,** 1040–1044

5. Guskov, A., Kern, J., Gabdulkhakov, A., Broser, M., Zouni, A., and Saenger, W. (2009) Cyanobacterial photosystem II at 2.9 Å resolution and the role of quinones, lipids, channels, and chloride. *Nat. Struct. Mol. Biol.* **16,** 334–342

6. Umena, Y., Kawakami, K., Shen, J. R., and Kamiya, N. (2011) Crystal structure of oxygen-evolving photosystem II at a resolution of 1.9 Å. *Nature* **473,** 55–60

7. Lubitz, W., Reijerse, E. J., and Messinger, J. (2008) Solar water-splitting into H_2 and O_2. Design principles of photosystem II and hydrogenases. *Energy Environ. Sci.* **1,** 15

8. Dau, H., and Zaharieva, I. (2009) Principles, efficiency, and blueprint character of solar-energy conversion in photosynthetic water oxidation. *Acc. Chem. Res.* **42,** 1861–1870

9. Messinger, J., and Renger, G. (2008) in *Primary Processes of Photosynthesis, Part 2: Principles and Apparatus* (Renger, G., ed.) pp. 291–349, Royal Society of Chemistry, Cambridge

10. Renger, G., and Renger, T. (2008) Photosystem II. The machinery of photosynthetic water splitting. *Photosynth. Res.* **98,** 53–80

11. McEvoy, J. P., and Brudvig, G. W. (2006) Water-splitting chemistry of photosystem II. *Chem. Rev.* **106,** 4455–4483

12. Nelson, N., and Yocum, C. F. (2006) Structure and function of photosystems I and II. *Annu. Rev. Plant Biol.* **57,** 521–565

13. Hillier, W., and Messinger, J. (2005) in *Photosystem II: The Light-Driven Water:Plastoquinone Oxidoreductase* (Wydrzynski, T. J., and Satho, K., eds.) pp. 567–608, Springer, Dordrecht

14. Messinger, J., Noguchi, T., and Yano, J. (2012) in *Molecular Solar Fuels*, RSC Energy and Environment Series (Wydrzynski, T. J., and Hillier, W., eds.) pp. 163–207, Royal Society of Chemistry, Cambridge

15. Yano, J., Kern, J., Irrgang, K. D., Latimer, M. J., Bergmann, U., Glatzel, P., Pushkar, Y., Biesiadka, J., Loll, B., Sauer, K., Messinger, J., Zouni, A., and Yachandra, V. K. (2005) X-ray damage to the Mn_4Ca complex in single crystals of photosystem II. A case study for metalloprotein crystallography. *Proc. Natl. Acad. Sci. U.S.A.* **102,** 12047–12052

16. Kusunoki, M. (2007) Mono-manganese mechanism of the photosystem II water splitting reaction by a unique Mn_4Ca cluster. *Biochim. Biophys. Acta* **1767,** 484–492

17. Siegbahn, P. E. (2009) Structures and energetics for O_2 formation in photosystem II. *Acc. Chem. Res.* **42,** 1871–1880

18. Ames, W., Pantazis, D. A., Krewald, V., Cox, N., Messinger, J., Lubitz, W., and Neese, F. (2011) Theoretical evaluation of structural models of the S_2 state in the oxygen evolving complex of photosystem II. Protonation states and magnetic interactions. *J. Am. Chem. Soc.* **133,** 19743–19757

19. Ghanotakis, D. F., Babcock, G. T., and Yocum, C. F. (1984) Calcium reconstitutes high rates of oxygen evolution in polypeptide depleted photosystem II preparations. *FEBS Letts.* **167,** 127–130

20. Ghanotakis, D. F., Topper, J. N., Babcock, G. T., and Yocum, C. F. (1984) Water-soluble 17- and 23-kDa polypeptides restore oxygen evolution activity by creating a high affinity binding site for Ca^{2+} on the oxidizing side of photosystem II. *FEBS Lett.* **170,** 169–173

21. Ono, T., and Inoue, Y. (1988) Discrete extraction of the Ca^{2+} atom functional for O_2 evolution in higher plant photosystem II by a simple low pH treatment. *FEBS Lett.* **227,** 147–152

22. Boussac, A., Maison-Peteri, B., Etienne, A. L., and Vernotte, C. (1985) Reactivation of oxygen evolution of NaCl-washed photosystem II parti-cles by Ca^{2+} and/or the 24-kDa protein. *Biochim. Biophys. Acta Bioenerg.* **808,** 231–234

23. Boussac, A., and Rutherford, A. W. (1988) Nature of the inhibition of the oxygen-evolving enzyme of photosystem II induced by NaCl washing and reversed by the addition of Ca^{2+} or Sr^{2+}. *Biochemistry* **27,** 3476–3483

24. Boussac, A., Zimmermann, J. L., and Rutherford, A. W. (1989) EPR signals from modified charge accumulation states of the oxygen evolving enzyme in Ca^{2+}-deficient photosystem II. *Biochemistry* **28,** 8984–8989

25. Sivaraja, M., Tso, J., and Dismukes, G. C. (1989) A calcium-specific site influences the structure and activity of the manganese cluster responsible for photosynthetic water oxidation. *Biochemistry* **28,** 9459–9464

26. Miqyass, M., van Gorkom, H. J., and Yocum, C. F. (2007) The PSII calcium site revisited. *Photosynth. Res.* **92,** 275–287

27. Yocum, C. F. (2008) The calcium and chloride requirements of the O_2 evolving complex. *Coord. Chem. Rev.* **252,** 296–305

28. Yachandra, V. K., and Yano, J. (2011) Calcium in the oxygen-evolving complex. Structural and mechanistic role determined by X-ray spectroscopy. *J. Photochem. Photobiol. B* **104,** 51–59

29. Latimer, M. J., DeRose, V. J., Yachandra, V. K., Sauer, K., and Klein, M. P. (1998) Structural effects of calcium depletion on the manganese cluster of photosystem II. Determination by x-ray absorption spectroscopy. *J. Phys. Chem. B* **102,** 8257–8265

30. Diner, B. A., and Britt, R. D. (2005) in *Photosystem II: The Light-Driven Water:Plastoquinone Oxidoreductase* (Wydrzynski, T. J., and Satoh, K., eds.) pp. 207–233, Springer, Dordrecht

31. Vrettos, J. S., Stone, D. A., and Brudvig, G. W. (2001) Quantifying the ion selectivity of the Ca^{2+} site in photosystem II. Evidence for direct involvement of Ca^{2+} in O_2 formation. *Biochemistry* **40,** 7937–7945

32. Boussac, A., Rappaport, F., Carrier, P., Verbavatz, J. M., Gobin, R., Kirilovsky, D., Rutherford, A. W., and Sugiura, M. (2004) Biosynthetic Ca^{2+}/Sr^{2+} exchange in the photosystem II oxygen-evolving enzyme of *Thermosynechococcus elongatus*. *J. Biol. Chem.* **279,** 22809–22819

33. Dismukes, G. C., and Siderer, Y. (1981) Intermediates of a polynuclear manganese center involved in photosynthetic oxidation of water. *Proc. Natl. Acad. Sci. U.S.A.* **78,** 274–278

34. Casey, J. L., and Sauer, K. (1984) EPR detection of a cryogenically photogenerated intermediate in photosynthetic oxygen evolution. *Biochim. Biophys. Acta Bioenerg.* **767,** 21–28

35. Zimmermann, J. L., and Rutherford, A. W. (1984) EPR studies of the oxygen-evolving enzyme of photosystem II. *Biochim. Biophys. Acta Bioenerg.* **767,** 160–167

36. Horner, O., Rivière, E., Blondin, G., Un, S., Rutherford, A. W., Girerd, J. J., and Boussac, A. (1998) SQUID magnetization study of the infrared-induced spin transition in the infrared-induced spin transition in the S_2 state of photosystem II. Spin value associated with the $g = 4.1$ EPR signal. *J. Am. Chem. Soc.* **120,** 7924–7928

37. Boussac, A. (1997) Inhomogeneity of the EPR multiline signal from the S_2 state of the photosystem II oxygen-evolving enzyme. *J. Biol. Inorg. Chem.* **2,** 580–585

38. Åhrling, K. A., Evans, M. C., Nugent, J. H., and Pace, R. J. (2004) The two forms of the S_2 state multiline signal in photosystem II. Effect of methanol and ethanol. *Biochim. Biophys. Acta* **1656,** 66–77

39. Force, D. A., Randall, D. W., Lorigan, G. A., Clemens, K. L., and Britt, R. D. (1998) ESEEM studies of alcohol binding to the manganese cluster of the oxygen-evolving complex of photosystem II. *J. Am. Chem. Soc.* **120,** 13321–13333

40. Åhrling, K. A., Evans, M. C., Nugent, J. H., Ball, R. J., and Pace, R. J. (2006) ESEEM studies of substrate water and small alcohol binding to the oxygen-evolving complex of photosystem II during functional turnover. *Biochemistry* **45,** 7069–7082

41. Su, J. H., Cox, N., Ames, W., Pantazis, D. A., Rapatskiy, L., Lohmiller, T., Kulik, L. V., Dorlet, P., Rutherford, A. W., Neese, F., Boussac, A., Lubitz, W., and Messinger, J. (2011) The electronic structures of the S_2 states of the oxygen-evolving complexes of photosystem II in plants and cyanobacteria in the presence and absence of methanol. *Biochim. Biophys. Acta* **1807,** 829–840

42. Peloquin, J. M., Campbell, K. A., Randall, D. W., Evanchik, M. A., Pec-

oraro, V. L., Armstrong, W. H., and Britt, R. D. (2000) ^{55}Mn ENDOR of the S$_2$-state multiline EPR signal of photosystem II. Implications on the structure of the tetranuclear Mn cluster. *J. Am. Chem. Soc.* **122,** 10926 –10942

43. Lorigan, G. A., and Britt, R. D. (1994) Temperature-dependent pulsed electron paramagnetic resonance studies of the S$_2$ state multiline signal of the photosynthetic oxygen-evolving complex. *Biochemistry* **33,** 12072–12076

44. Kulik, L., Epel, B., Messinger, J., and Lubitz, W. (2005) Pulse EPR, ^{55}Mn-ENDOR, and ELDOR-detected NMR of the S$_2$-state of the oxygen evolving complex in photosystem II. *Photosynth. Res.* **84,** 347–353

45. Kulik, L. V., Epel, B., Lubitz, W., and Messinger, J. (2005) ^{55}Mn pulse ENDOR at 34 GHz of the S$_0$ and S$_2$ states of the oxygen-evolving complex in photosystem II. *J. Am. Chem. Soc.* **127,** 2392–2393

46. Kulik, L. V., Epel, B., Lubitz, W., and Messinger, J. (2007) Electronic structure of the Mn$_4$O$_x$Ca cluster in the S$_0$ and S$_2$ states of the oxygen-evolving complex of photosystem II based on pulse ^{55}Mn-ENDOR and EPR spectroscopy. *J. Am. Chem. Soc.* **129,** 13421–13435

47. Pantazis, D. A., Orio, M., Petrenko, T., Zein, S., Lubitz, W., Messinger, J., and Neese, F. (2009) Structure of the oxygen-evolving complex of photosystem II. Information on the S$_2$ state through quantum chemical calculation of its magnetic properties. *Phys. Chem. Chem. Phys.* **11,** 6788 – 6798

48. Teutloff, C., Pudollek, S., Kessen, S., Broser, M., Zouni, A., and Bittl, R. (2009) Electronic structure of the tyrosine D radical and the water-splitting complex from pulsed ENDOR spectroscopy on photosystem II single crystals. *Phys. Chem. Chem. Phys.* **11,** 6715 – 6726

49. Cox, N., Rapatskiy, L., Su, J. H., Pantazis, D. A., Sugiura, M., Kulik, L., Dorlet, P., Rutherford, A. W., Neese, F., Boussac, A., Lubitz, W., and Messinger, J. (2011) Effect of Ca^{2+}/Sr^{2+} substitution on the electronic structure of the oxygen-evolving complex of photosystem II. A combined multifrequency EPR, ^{55}Mn-ENDOR, and DFT study of the S$_2$ state. *J. Am. Chem. Soc.* **133,** 3635–3648

50. Stich, T. A., Yeagle, G. J., Service, R. J., Debus, R. J., and Britt, R. D. (2011) Ligation of D1-His-332 and D1-Asp-170 to the manganese cluster of photosystem II from *Synechocystis* assessed by multifrequency pulse EPR spectroscopy. *Biochemistry* **50,** 7390 –7404

51. Booth, P. J., Rutherford, A. W., and Boussac, A. (1996) Location of the calcium binding site in photosystem II. A Mn^{2+} substitution study. *Biochim. Biophys. Acta Bioenerg.* **1277,** 127–134

52. Berthold, D. A., Babcock, G. T., and Yocum, C. F. (1981) A highly resolved, oxygen-evolving photosystem II preparation from spinach thylakoid membranes. EPR and electron-transport properties. *FEBS Lett.* **134,** 231–234

53. Arnon, D. I. (1949) Copper enzymes in isolated chloroplasts. Polyphenoloxidase in β-vulgaris. *Plant Physiol.* **24,** 1–15

54. Porra, R. J., Thompson, W. A., and Kriedemann, P. E. (1989) Determination of accurate extinction coefficients and simultaneous equations for assaying chlorophylls *a* and *b* extracted with four different solvents. Verification of the concentration of chlorophyll standards by atomic absorption spectroscopy. *Biochim. Biophys. Acta Bioenerg.* **975,** 384–394

55. Cinco, R. M., Robblee, J. H., Rompel, A., Fernandez, C., Yachandra, V. K., Sauer, K., and Klein, M. P. (1998) Strontium EXAFS reveals the proximity of calcium to the manganese cluster of oxygen-evolving photosystem II. *J. Phys. Chem. B* **102,** 8248 – 8256

56. Ono, T., and Inoue, Y. (1989) Roles of Ca^{2+} in O$_2$ evolution in higher plant photosystem II. Effects of replacement of Ca^{2+} site by other cations. *Arch. Biochem. Biophys.* **275,** 440 – 448

57. Roberts, A. G., Gregor, W., Britt, R. D., and Kramer, D. M. (2003) Acceptor and donor-side interactions of phenolic inhibitors in photosystem II. *Biochim. Biophys. Acta* **1604,** 23–32

58. Reijerse, E., Lendzian, F., Isaacson, R., and Lubitz, W. (2012) A tunable general purpose Q-band resonator for CW and pulse EPR/ENDOR experiments with large sample access and optical excitation. *J. Magn. Reson.* **214,** 237–243

59. Epel, B., Gromov, I., Stoll, S., Schweiger, A., and Goldfarb, D. (2005) Spectrometer manager. A versatile control software for pulse EPR spectrometers *Concepts Magn. Reson. Part B (Magn. Reson. Engineering)* **26B,** 36 – 45

60. Stoll, S., and Schweiger, A. (2006) EasySpin, a comprehensive software package for spectral simulation and analysis in EPR. *J. Magn. Reson.* **178,** 42–55

61. Sturgeon, B. E., Ball, J. A., Randall, D. W., and Britt, R. D. (1994) ^{55}Mn electron spin echo ENDOR of Mn^{2+} Complexes. *J. Phys. Chem.* **98,** 12871–12883

62. Rutherford, A. W., and Zimmermann, J. L. (1984) A new EPR signal attributed to the primary plastosemiquinone acceptor in photosystem II. *Biochim. Biophys. Acta Bioenerg.* **767,** 168 –175

63. Zheng, M., and Dismukes, G. C. (1996) Orbital configuration of the valence electrons, ligand field symmetry, and manganese oxidation states of the photosynthetic water oxidizing complex. Analysis of the S$_2$ state multiline EPR signals. *Inorg. Chem.* **35,** 3307–3319

64. Kusunoki, M. (1992) A new paramagnetic hyperfine structure effect in manganese tetramers. The origin of "multiline" EPR signals from an S$_2$ state of a photosynthetic water-splitting enzyme. *Chem. Phys. Lett.* **197,** 108 –116

65. Charlot, M. F., Boussac, A., and Blondin, G. (2005) Toward a spin coupling model for the Mn$_4$ cluster in photosystem II. *Biochim. Biophys. Acta* **1708,** 120 –132

66. Teutloff, C., Kessen, S., Kern, J., Zouni, A., and Bittl, R. (2006) High-field (94 GHz) EPR spectroscopy on the S$_2$ multiline signal of photosystem II. *FEBS Lett.* **580,** 3605 –3609

67. Lohmiller, T., Cox, N., Su, J. H., Messinger, J., and Lubitz, W. (2010) *Proceedings of 15th International Congress on Photosynthesis* Beijing, China, August 22–27, 2010, Zhejiang University Press/Springer, Dordrecht

68. Murray, J. W., and Barber, J. (2006) Identification of a calcium-binding site in the PsbO protein of photosystem II. *Biochemistry* **45,** 4128 – 4130

69. Zhang, L. X., Liang, H. G., Wang, J., Li, W. R., and Yu, T. Z. (1996) Fluorescence and Fourier-transform infrared spectroscopic studies on the role of disulfide bond in the calcium binding in the 33-kDa protein of photosystem II. *Photosynth. Res.* **48,** 379 –384

70. Heredia, P., and De Las Rivas, J. (2003) Calcium-dependent conformational change and thermal stability of the isolated PsbO protein detected by FTIR spectroscopy. *Biochemistry* **42,** 11831–11838

71. Kruk, J., Burda, K., Jemioła-Rzemińska, M., and Strzałka, K. (2003) The 33-kDa protein of photosystem II is a low affinity calcium- and lanthanide-binding protein. *Biochemistry* **42,** 14862–14867

72. Abramowicz, D. A., and Dismukes, G. C. (1984) Manganese proteins isolated from spinach thylakoid membranes and their role in O$_2$ evolution. II. A binuclear manganese-containing 34-kilodalton protein, a probable component of the water dehydrogenase enzyme. *Biochim. Biophys. Acta* **765,** 318 –328

73. Yamamoto, Y., Shinkai, H., Isogai, Y., Matsuura, K., and Nishimura, M. (1984) Isolation of an Mn-carrying 33-kDa protein from an oxygen-evolving photosystem-II preparation by phase partitioning with butanol. *FEBS Lett.* **175,** 429 – 432

74. Lu, Y. K., Theg, S. M., and Stemler, A. J. (2005) Carbonic anhydrase activity of the photosystem II OEC33 protein from pea. *Plant Cell Physiol.* **46,** 1944 –1953

75. Bondarava, N., Beyer, P., and Krieger-Liszkay, A. (2005) Function of the 23-kDa extrinsic protein of photosystem II as a manganese-binding protein and its role in photoactivation. *Biochim. Biophys. Acta* **1708,** 63–70

76. Bondarava, N., Un, S., and Krieger-Liszkay, A. (2007) Manganese binding to the 23-kDa extrinsic protein of photosystem II. *Biochim. Biophys. Acta* **1767,** 583–588

77. Bricker, T. M., and Frankel, L. K. (2011) Auxiliary functions of the PsbO, PsbP, and PsbQ proteins of higher plant photosystem II. A critical analysis. *J. Photochem. Photobiol. B* **104,** 165–178

78. Michoux, F., Takasaka, K., Boehm, M., Nixon, P. J., and Murray, J. W. (2010) Structure of CyanoP at 2.8 Å. Implications for the evolution and function of the PsbP subunit of photosystem II. *Biochemistry* **49,** 7411–7413

79. Dasgupta, J., Ananyev, G. M., and Dismukes, G. C. (2008) Photoassembly of the water-oxidizing complex in photosystem II. *Coord. Chem. Rev.* **252,** 347–360

80. Mulo, P., Sirpiö, S., Suorsa, M., and Aro, E. M. (2008) Auxiliary proteins involved in the assembly and sustenance of photosystem II. *Photosynth. Res.* **98,** 489–501

81. Grasse, N., Mamedov, F., Becker, K., Styring, S., Rögner, M., and Nowaczyk, M. M. (2011) Role of novel dimeric photosystem II (PSII)-Psb27 protein complex in PSII repair. *J. Biol. Chem.* **286,** 29548–29555

82. Komenda, J., Michoux, F., and Nixon, P. (2011) in *Self-Healing at the Nanoscale*, pp. 3–22, CRC Press

83. Pace, R. J., Smith, P., Bramley, R., and Stehlik, D. (1991) EPR saturation and temperature dependence studies on signals from the oxygen-evolving centre of photosystem II. *Biochim. Biophys. Acta Bioenerg.* **1058,** 161–170

84. Åhrling, K. A., Peterson, S., and Styring, S. (1998) The S_0 state EPR signal from the Mn cluster in photosystem II arises from an isolated $S = 1/2$ ground state. *Biochemistry* **37,** 8115–8120

85. Siegbahn, P. E. (2009) Water oxidation in photosystem II. Oxygen release, proton release, and the effect of chloride. *Dalton Trans.* 45, 10063–10068

86. Griffith, J. S. (2009) *The Theory of Transition-Metal Ions*, Cambridge University Press, Cambridge, UK

87. Gerritsen, H. J., and Sabisky, E. S. (1963) Paramagnetic resonance of trivalent manganese in rutile (TiO_2). *Phys. Rev.* **132,** 1507–1512

88. Campbell, K. A., Force, D. A., Nixon, P. J., Dole, F., Diner, B. A., and Britt, R. D. (2000) Dual-mode EPR detects the initial intermediate in photoassembly of the photosystem II Mn cluster. The influence of amino acid residue 170 of the D1 polypeptide on Mn coordination. *J. Am. Chem. Soc.* **122,** 3754–3761

89. Baldwin, M. J., Stemmler, T. L., Riggs-Gelasco, P. J., Kirk, M. L., Penner-Hahn, J. E., and Pecoraro, V. L. (1994) Structural and magnetic effects of successive protonations of oxo bridges in high-valent manganese dimers. *J. Am. Chem. Soc.* **116,** 11349–11356

90. Yano, J., Kern, J., Sauer, K., Latimer, M. J., Pushkar, Y., Biesiadka, J., Loll, B., Saenger, W., Messinger, J., Zouni, A., and Yachandra, V. K. (2006) Where water is oxidized to dioxygen: structure of the photosynthetic Mn₄Ca cluster. *Science* **314,** 821–825

91. Pushkar, Y., Yano, J., Glatzel, P., Messinger, J., Lewis, A., Sauer, K., Bergmann, U., and Yachandra, V. (2007) Structure and orientation of the Mn₄Ca cluster in plant photosystem II membranes studied by polarized range-extended x-ray absorption spectroscopy. *J. Biol. Chem.* **282,** 7198–7208

92. Tso, J., Sivaraja, M., and Dismukes, G. C. (1991) Calcium limits substrate accessibility or reactivity at the manganese cluster in photosynthetic water oxidation. *Biochemistry* **30,** 4734–4739

93. Boussac, A., and Rutherford, A. W. (1988) Ca²⁺ binding to the oxygen evolving enzyme varies with the redox state of the Mn cluster. *FEBS Lett.* **236,** 432–436

94. Lavergne, J., and Junge, W. (1993) Proton release during the redox cycle of the water oxidase. *Photosynth. Res.* **38,** 279–296

95. Pecoraro, V. L., Baldwin, M. J., Caudle, M. T., Hsieh, W.-Y., and Law, N. A. (1998) A proposal for water oxidation in photosystem II. *Pure Appl. Chem.* **70,** 925–929

96. Messinger, J., Badger, M., and Wydrzynski, T. (1995) Detection of one slowly exchanging substrate water molecule in the S_3 state of photosystem II. *Proc. Natl. Acad. Sci. U.S.A.* **92,** 3209–3213

97. Dau, H., and Haumann, M. (2008) The manganese complex of photosystem II in its reaction cycle. Basic framework and possible realization at the atomic level. *Coord. Chem. Rev.* **252,** 273–295

98. Yachandra, V. K. (2005) in *Photosystem II: The Light-Driven Water: Plastoquinone Oxidoreductase* (Wydrzynski, T. J., and Satoh, K., eds.) pp. 235–260, Springer, Dordrecht

99. Hillier, W., and Wydrzynski, T. (2008) ¹⁸O-water exchange in photosystem II. Substrate binding and intermediates of the water splitting cycle. *Coord. Chem. Rev.* **252,** 306–317

100. Messinger, J., Robblee, J. H., Bergmann, U., Fernandez, C., Glatzel, P., Visser, H., Cinco, R. M., McFarlane, K. L., Bellacchio, E., Pizarro, S. A., Cramer, S. P., Sauer, K., Klein, M. P., and Yachandra, V. K. (2001) Absence of Mn-centered oxidation in the $S_2 \rightarrow S_3$ transition. Implications for the mechanism of photosynthetic water oxidation. *J. Am. Chem. Soc.* **123,** 7804–7820

SUPPLEMENTAL DATA

The Basic Properties of the Electronic Structure of the Oxygen-Evolving Complex of Photosystem II are not Perturbed by Ca²⁺ Removal

Thomas Lohmiller,[‡] Nicholas Cox,[‡] Ji-Hu Su,[‡,§] Johannes Messinger,[‖] Wolfgang Lubitz[‡,1]

[‡]Max-Planck-Institut für Bioanorganische Chemie, Stiftstrasse 34-36, 45470 Mülheim an der Ruhr, Germany.

[§]Present address: Department of Modern Physics, University of Science and Technology of China, Hefei, Anhui 230026, China.

[‖]Department of Chemistry, Chemical Biological Centre (KBC), Umeå University, S-90187 Umeå, Sweden.

[1]To whom correspondence should be addressed: Prof. Dr. Wolfgang Lubitz, Max-Planck-Institut für Bioanorganische Chemie, Stiftstrasse 34-36, 45470 Mülheim an der Ruhr, Germany, Tel: +49 208 306 3614. Fax: +49 208 306 3955. E-mail: wolfgang.lubitz@mpi-mail.mpg.de.
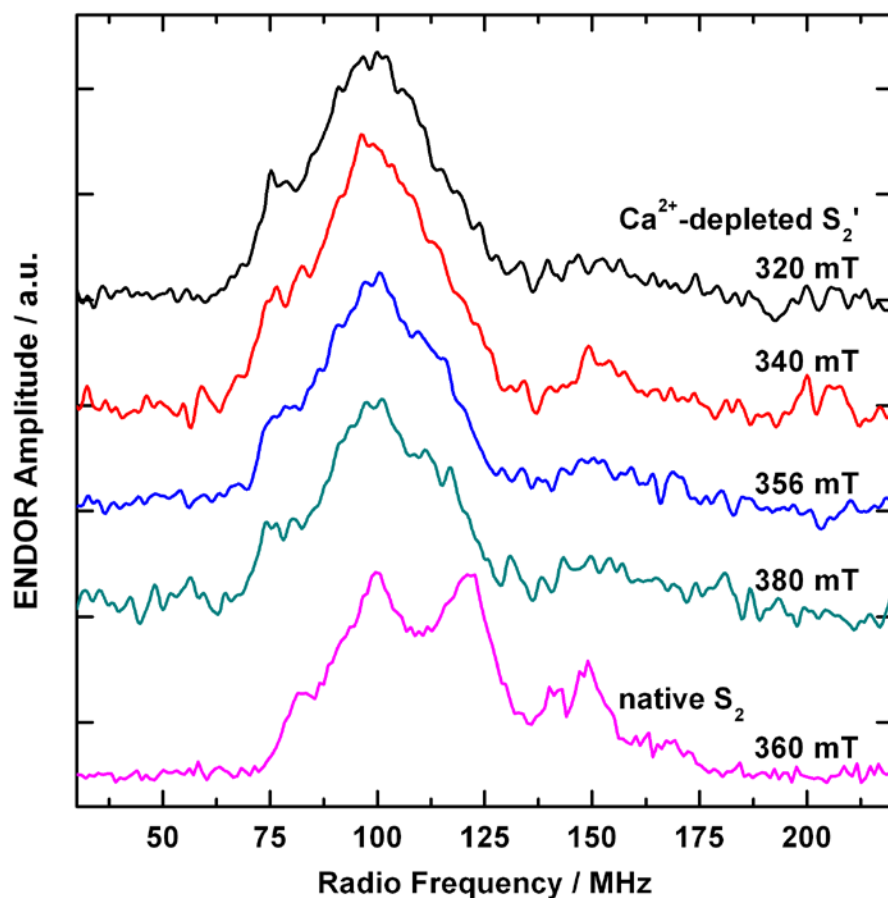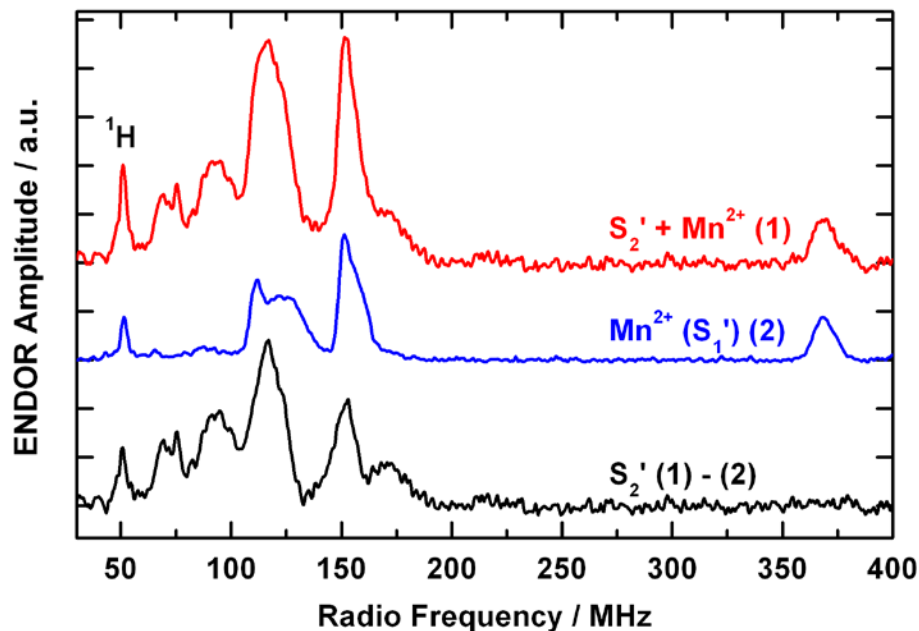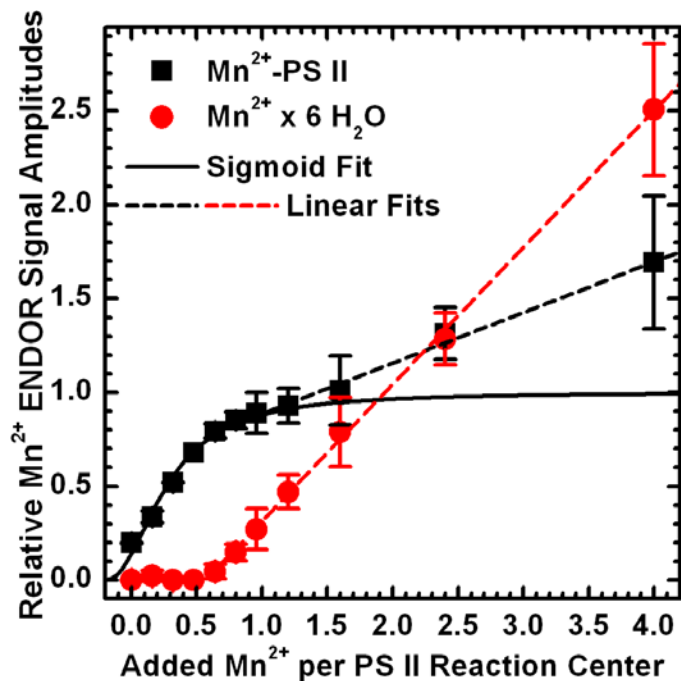
SUPPLEMENTAL FIGURE S1. X-band Davies ENDOR spectra of the Ca^{2+}-depleted OEC poised in the S$_2'$ state in PS II isolated from spinach at various magnetic fields and, for comparison, of the native OEC in the S$_2$ state in the presence of 3 % MeOH at $B_0 = 360$ mT (bottom trace), as published in Refs. (1, 2). The S$_2'$ state spectra were smoothed using a 9-point moving average. Experimental parameters (S$_2'$ state): MW frequency: 9.717 GHz; shot repetition rate: 5 µs; MW pulse length π: 12 ns; τ: 200 ns; magnetic fields B_0: 320 mT, 340 mT, 356 mT, 380 mT (from the top); RF pulse length π_{RF}: 4 µs; temperature: 5 K; accumulations/time: 460/355 min, 166/149 min, 160/144 min, 339/305 min (from the top).

SUPPLEMENTAL FIGURE S2. Q-band Davies ENDOR spectra of Ca^{2+}-depleted PS II isolated from spinach illustrating the subtraction of the contaminating Mn^{2+} signal from the raw data obtained from the sample poised in the S$_2'$ state, which yields the pure spectrum of the Ca^{2+}-depleted Mn$_4$O$_5$ cluster in the S$_2'$ state. Top trace (1): Spectrum of an illuminated sample poised in the S$_2'$ state containing both the S$_2'$ state signal and contributions from residual Mn^{2+} ions. Middle trace (2): Spectrum of a dark-adapted sample poised in the S$_1'$ state before illumination showing only the Mn^{2+} signal. For the subtraction, both spectra (1) and (2) were normalized with respect to the signal around 370 MHz, to which only the Mn^{2+} ion contributes. Bottom trace (1 – 2): difference of the spectra from samples in the S$_2'$ and the S$_1'$ states, the result of which is the spectrum of the OEC in the S$_2'$ state. Experimental settings: MW frequency: 34.033 GHz; shot repetition rate: 5 µs; MW pulse length π: 72 ns; τ: 480 ns; magnetic field B_0: 1208 mT; RF pulse length π_{RF}: 4 µs; temperature: 5 K; accumulations/time: 202/218 min (1), 358/387 min (2).

SUPPLEMENTAL FIGURE S3. Titration of dark-adapted Ca^{2+}-depleted PS II samples (S$_1'$ state) with Mn^{2+}. The relative Q-band ^{55}Mn Davies ENDOR signal intensities of Mn^{2+} ions bound to the PS II protein complex (black squares) and hexaquo-Mn^{2+} in solution (red circles), quantified as described in the Experimental Procedures section 2.6 (main text), are plotted against the equivalents of Mn^{2+} ions added to the samples. The concentration of the defined PS II-bound Mn^{2+} species as a function of added Mn^{2+} was reproduced by means of a sigmoid curve fitted to the determined intensities up to 1.2 equivalents of Mn^{2+} in which the zero crossing of the x-axis was shifted to -0.2 equivalents with a half-binding value of 0.47 equivalents (solid line). The increase of hexaquo-Mn^{2+}, as well as additionally unspecifically bound hexaquo-Mn^{2+} ions was reproduced by linear fits to the measured intensities above 0.64 equivalents of added Mn^{2+} ions (dashed lines). The concentration of reaction centers in the samples was 25 ± 3 µM. For the experimental parameters of the ^{55}Mn Davies ENDOR measurements see Fig. 4A (main text).

```
T. vulcanus        1    ------------------------------------------------------------      0
T. elongatus       1    ---------------------------------------------MKYRILMATLLAV     13
Spinacea oleracea  1    MAASLQASTTFLQPTKVASRNTLQLRSTQNVCKAFGVESASSGGRLSLSLQSDLKELANK     60

T. vulcanus        1    ---------------------------------TLTYDDIVGTGLANKCPTLDDTAR      24
T. elongatus      14    CLGIFSL-------------------SAPAFAAKQTLTYDDIVGTGLANKCPTLDDTAR     53
Spinacea oleracea 61    CVDATKLAGLALATSALIASGANAEGGKRLTYDEIQSKTYLEVKGTGTANQCPTVEGGVD    120

T. vulcanus       25    GAYPIDSSQTYRIARLCLQPTTFLVKEEPKNKRQEAEFVPTKLVTRETTSLDQIQGELKV     84
T. elongatus      54    GAYPIDSSQTYRIARLCLQPTTFLVKEEPKNKRQEAEFVPTKLVTRETTSLDQIQGELKV    113
Spinacea oleracea 121   SF-A-FKPGKYTAKKFCLEPTKFAVKAEGISKNSGPDFQNTKLMTRLTYTLDEIEGPFEV    178

T. vulcanus       85    NSDGSLTFVEEDGIDFQPVTVQMAGGERIPLLFTVKNLVASTQPNVTSITTSTDFKGEFN    144
T. elongatus     114    NSDGSLTFVEEDGIDFQPVTVQMAGGERIPLLFTVKNLVASTQPNVTSITTSTDFKGEFN    173
Spinacea oleracea 179   SSDGTVKFEEKDGIDYAAVTVQLPGGERVPFLFTIKQLVASGKPE--------SFSGDFL    230

T. vulcanus      145    VPSYRTANFLDPKGRGLASGYDSAIALPQA---KEEELARANVKRFSLTKGQISLNVAKV    201
T. elongatus     174    VPSYRTANFLDPKGRGLASGYDSAIALPQA---KEEELARANVKRFSLTKGQISLNVAKV    230
Spinacea oleracea 231   VPSYRGSSFLDPKGRGGSTGYDNAVALPAGGRGDEEELQKENNKNVASSKGTITLSVTSS    290

T. vulcanus      202    DGRTGEIAGTFESEQLSDDDMGAHEPHEVKIQGVFYASIEP-    242
T. elongatus     231    DGRTGEIAGTFESEQLSDDDMGAHEPHEVKIQGVFYASIEPA    272
Spinacea oleracea 291   KPETGEVIGVFQSLQPSDTDLGAKVPKDVKIEGVWYAQLEQQ    332
```

SUPPLEMENTAL FIGURE S4. Amino acid sequence alignment of the PsbO proteins from the cyanobacteria *T. vulcanus* and *T. elongatus* and the higher plant spinach (*Spinacea oleracea*). Residues ligating the Ca^{2+} ions at the sites identified in the PS II crystal structures from *T. vulcanus* and *T. elongatus* are highlighted in red and blue, respectively. The protein sequence alignment was performed using the BLAST search engine provided by UniProt (3).

SUPPLEMENTAL TABLE S1. Principal Values[a] and Isotropic[b] and Anisotropic[c] Values of the Effective G and ^{55}Mn HFI Tensors A_i (i = 1-4) for the Simulations of the X- and Q-Band EPR and ENDOR Spectra of the Ca^{2+}-depleted PS II from Spinach in the S$'_2$ State (Fig. 2, Main Text) and for the S$_2$ States of Native Spinach PS II (2) and Native and Sr^{2+}-substituted PS II from *T. elongatus* (4).

			G	A_1 / MHz	A_2 / MHz	A_3 / MHz	A_4 / MHz
Spinach	-Ca^{2+} S$'_2$	x	1.979	342	212	173	139
		y	1.986	328	199	205	164
		$\perp$ [a]	1.983	335	206	189	152
		z ($\parallel$) [a]	1.979	263	290	227	211
		iso [b]	1.981	311	234	202	171
		aniso [c]	0.004	72	-84	-38	-59
	Ca^{2+} S$_2$	x	1.997	310	235	185	170
		y	1.970	310	235	185	170
		$\perp$ [a]	1.984	310	235	185	170
		z ($\parallel$)	1.965	275	275	245	240
		iso	1.977	298	248	205	193
		aniso	0.019	35	-40	-60	-70
T. elongatus	Ca^{2+} S$_2$	x	1.971	350	249	202	148
		y	1.948	310	227	182	162
		$\perp$ [a]	1.960	330	238	192	155
		z ($\parallel$)	1.985	275	278	240	263
		iso	1.968	312	251	208	191
		aniso	-0.025	55	-40	-48	-108
	Sr^{2+} S$_2$	x	1.995	343	244	200	156
		y	1.968	361	217	185	152
		$\perp$ [a]	1.982	352	231	193	154
		z ($\parallel$)	1.957	293	268	223	210
		iso	1.973	332	243	203	173
		aniso	0.025	59	-37	-30	-56

[a] The equatorial and axial G and A_i values are defined as $G_\perp = (G_x+G_y)/2$, $G_\parallel = G_z$ and $A_{i,\perp} = (A_{i,x}+A_{i,y})/2$, $A_{i,\parallel} = A_{i,z}$. [b] The isotropic G_{iso} and $A_{i,iso}$ (i = 1-4) values are the averages of the principal values: $G_{iso} = (G_x+G_y+G_z)/3$ and $A_{i,iso} = (A_{i,x}+A_{i,y}+A_{i,z})/3$. [c] The anisotropy in the G and A_i values is expressed as the differences $G_{aniso} = G_\perp - G_\parallel$ and $A_{i,aniso} = A_\perp - A_\parallel$ between the perpendicular and parallel components of the tensors.

Correlation between the ground-to-first excited state energy difference Δ and the temperature dependence of the intensity I_1 of the ground spin state EPR signal. The relative intensity I_1 of the ground spin state signal I_1 depends on the inverse temperature weighted by the Boltzmann factor:

$$I_1 = \frac{C}{T} \frac{(2S_1 + 1)\exp(-E_1/kT)}{\sum_i (2S_i + 1)\exp(-E_i/kT)} \tag{S1}$$

where C is a proportionality constant, S_i represents the total spin of the coupled states of the spin manifold (S = 1/2, 3/2, …..) and E_i are the respective energies. Here, a two spin model is used to describe the energy ladder in terms of a single effective coupling constant, J_{eff} between two fragments of the Mn tetramer: monomeric Mn$_{A4}$ (Mn^{IV}, S_{A4} = 3/2), and the coupled trimer Mn$_{B3}$Mn$_{C2}$Mn$_{D1}$ (Mn^{III}(Mn^{IV})$_2$, spin ground state $S_{B3\text{-}C2\text{-}D1}$ = 1 or 2), see (5). The corresponding simplified Hamiltonian $H = -J_{\text{eff}}S_{A4}S_{B3\text{-}C2\text{-}D1}$ gives spin state energies $E_i = (S_{A4}(S_{A4} + 1) + S_{B3\text{-}C2\text{-}D1}(S_{B3\text{-}C2\text{-}D1} + 1) - S_i(S_i + 1))$ J_{eff}, where the total spin $S_i = (S_{A4} - S_{B3\text{-}C2\text{-}D1})…(S_{A4} + S_{B3\text{-}C2\text{-}D1})$ = 1/2…5/2. Equation S1 can thus be used to estimate J_{eff} and $Δ = E_2 - E_1 = -3J_{\text{eff}}$.

Effect of the Zero-Field Splitting Interaction on the Spin States and EPR and ^{55}Mn ENDOR Signals of

Mn²⁺ Complexes (see also (6)*).* The EPR and ^{55}Mn ENDOR signals originating from the Mn^{2+} ions

bound to Ca^{2+}-depleted PS II differ substantially from those typically associated with mononuclear Mn^{2+}

species in that they appear significantly broadened by the large and strongly rhombic ZFS (Figs. 3 and

4A in the main text). The characteristic EPR spectrum of high-spin $S = 5/2$ Mn^{2+} complexes is the six-

line signal with a HFI splitting of ~9 mT. For the ^{55}Mn nucleus of nuclear spin $I = 5/2$, each of these

lines can be assigned to one nuclear spin sublevel m_I ranging from -5/2 to +5/2. The corresponding ^{55}Mn

ENDOR signal contains 3 orientation-selective doublets centered roughly around ~125, ~375 and ~625

MHz, which originate from nuclear transitions within the $m_S = |1/2|$, $|3/2|$ and $|5/2|$ electronic

submanifolds, respectively.

In the absence of a ZFS interaction, a ^{55}Mn^{2+} EPR spectrum consist of six separate lines associated

with one m_I sublevel, to each of which the five $\Delta m_S = \pm 1$ transitions contribute. The ZFS leads to an

anisotropic broadening of these transitions, especially those involving manifolds of electronic spin

substates $|m_S| > 1/2$. Additionally, the symmetry of the ZFS tensor has a considerable effect on the

orientation-dependence and thus on the line width. A large rhombicity of this interaction enhances the

broadening of the powder patterns. As the ZFS becomes more relevant, the transitions associated with a

certain m_I are increasingly overlapping, such that it comes to a spreading of the entire spectrum. To

some extent, the broadening may additionally be attributed to small site-to-site inhomogeneities of the

Mn^{2+} environment, which have an immediate effect on the spin Hamiltonian parameters and are

especially found in large and dynamic biological systems like proteins. These effects add up to result in

the very broad, featureless spectrum, in which the six-line hyperfine structure from $|m_S| = 1/2$ transitions

is not resolved.

The pulse ENDOR spectra are directly affected by this spread. In the absence of a ZFS, the transitions

involving a particular m_I can be probed individually by selective irradiation at frequency and field of one

of the six EPR lines. Therefore, six different ^{55}Mn ENDOR spectra can be measured, each of them only

comprising the transitions corresponding to the selected nuclear spin m_I, associated with all six m_S

sublevels. In case of a ZFS-induced anisotropic spread of the m_S substate energies, the relative intensities of the ENDOR lines from the six m_S substates for a particular m_I become orientation-selective. In Fig. 4 (main text), the high-frequency $m_S = -3/2$ signal intensities relative to those of the low-frequency $m_S = -1/2$ and $m_S = +1/2$ signals are clearly smaller at the more central field positions in the EPR spectrum, the spectra at 1208 mT and 1224 mT, compared to the outer ones. At 1195 mT and 1260 mT, there is a stronger relative contribution from the $m_S = -3/2$ transitions due to their larger spread by the ZFS. Furthermore, the overlapping transition energies of the different m_I manifolds result in spectra comprising the ENDOR transitions of more than one m_I value, which leads to a broadening and concomitant lowering of the structural resolution of ENDOR lines. This reduced m_I selectivity can be clearly seen in these very broad ^{55}Mn ENDOR spectra where no spectral structure of single m_I transitions is resolved. Due to the large energetic spread in the case of the high-spin $m_S = -3/2$ sublevels, even all five corresponding m_I transitions are excited at the same time.

The Electronic Structure of an Effective S = 1/2 Spin State System: Relation of Effective Tensor Properties and Non-Explicitly Treated Interaction Terms. For evaluation of the intrinsic ZFS values d_i of the Mn ions resulting from the obtained electronic exchange coupling scheme (Fig. 7 in the main text) and whether these are within the reasonable ranges for the individual Mn oxidation states, a short overview is given on how they are calculated based on the inferred coupling topology and experimental effective spin Hamiltonian parameters:

Same as for the Ca^{2+}- and Sr^{2+}-containing S$_2$ states, the coupled Mn electronic spin system of the Ca^{2+}-depleted S$_2'$ state can be described by an effective spin Hamiltonian (see the Experimental Procedures section 2.5), which does not include any pair-wise interaction terms such as the Heisenberg-Dirac-Van Vleck operator for the electronic exchange interaction and the ZFS term. Thus, the fitted G and HFI tensors A_i (Table 2 in the main text, supplemental Table S1) also represent effective tensors. However instead, the corresponding intrinsic (on-site) HFI tensors a_i need to be considered for comparison to values reported for other Mn systems, assignment of oxidation states and conclusions about coordination geometries of individual Mn ions. Effective and intrinsic properties of each Mn$_i$ ion are related by a spin projection coefficient ρ_i, a measure of the contribution of Mn$_i$ to a particular spin state. The tensor components of this scaling factor are the ratio of the corresponding effective and intrinsic values, i.e. $\rho_i = A_i / a_i$ for the HFI. The effective G tensor, as a property of the effective electron spin S of the Mn cluster, is a weighted linear sum of the intrinsic g tensors of the individual Mn ions $G = \sum \rho_i g_i$. As they map the subspace of the effective spin state to the entire configuration space, the ρ_i tensors for oligomeric spin systems can be computed based on the spin coupling scheme in the form of pair-wise electronic exchange interaction terms between all of the four Mn ions. Therein, the ZFS interaction, not considered explicitly as a term of the spin Hamiltonian, can be taken into account such that it affects the ρ_i tesors in an orientation-dependent manner. Through the exchange coupling between the electronic spins, the intrinsic ZFS value d_i of one Mn ion influences the ρ_j tensors of the others, too, which thus can be envisaged as a transfer of anisotropy to the other Mn ions in the cluster (for more detailed information see Refs. (4, 7, 8)).

REFERENCES

1. Kulik, L., Epel, B., Messinger, J., and Lubitz, W. (2005) *Photosynth. Res.* **84**, 347–353

2. Kulik, L. V., Epel, B., Lubitz, W., and Messinger, J. (2007) *J. Am. Chem. Soc.* **129**, 13421–13435

3. The UniProt Consortium (2011) *Nucleic Acids Res.* **40**, D71–D75

4. Cox, N., Rapatskiy, L., Su, J.-H., Pantazis, D. A., Sugiura, M., Kulik, L., Dorlet, P., Rutherford, A. W., Neese, F., Boussac, A., Lubitz, W., and Messinger, J. (2011) *J. Am. Chem. Soc.* **133**, 3635–3648

5. Su, J.-H., Cox, N., Ames, W., Pantazis, D. A., Rapatskiy, L., Lohmiller, T., Kulik, L. V., Dorlet, P., Rutherford, A. W., Neese, F., Boussac, A., Lubitz, W., and Messinger, J. (2011) *Biochim. Biophys. Acta, Bioenerg.* **1807**, 829–840

6. Sturgeon, B. E., Ball, J. A., Randall, D. W., and Britt, R. D. (1994) *J. Phys. Chem.* **98**, 12871–12883

7. Peloquin, J. M., Campbell, K. A., Randall, D. W., Evanchik, M. A., Pecoraro, V. L., Armstrong, W. H., and Britt, R. D. (2000) *J. Am. Chem. Soc.* **122**, 10926–10942

8. Schäfer, K.-O., Bittl, R., Zweygart, W., Lendzian, F., Haselhorst, G., Weyhermüller, T., Wieghardt, K., and Lubitz, W. (1998) *J. Am. Chem. Soc.* **120**, 13104–13120

The Basic Properties of the Electronic Structure of the Oxygen-evolving Complex of Photosystem II Are Not Perturbed by Ca $^{2+}$ Removal

Thomas Lohmiller, Nicholas Cox, Ji-Hu Su, Johannes Messinger and Wolfgang Lubitz

---

Access the most updated version of this article at doi: 10.1074/jbc.M112.365288

Alerts:
- When this article is cited
- When a correction for this article is posted

Click here to choose from all of JBC's e-mail alerts

Supplemental material:
http://www.jbc.org/content/suppl/2012/05/01/M112.365288.DC1.html

This article cites 92 references, 11 of which can be accessed free at
http://www.jbc.org/content/287/29/24721.full.html#ref-list-1